

# **SWEET**

## **User Manual**

### **Version 2.0**

S. Corti  
M. Marrocu  
L. Paglieri  
L. Trotta

©ENEL-Polo Idraulico e Strutturale - Milano, CRS4 - Cagliari  
October 1997



# Contents

<b>I</b>	<b>Physical Modeling</b>	<b>5</b>
<b>1</b>	<b>The 3D Navier–Stokes Equations</b>	<b>5</b>
<b>2</b>	<b>Shallow Water Model</b>	<b>6</b>
2.1	Continuity Equation . . . . .	7
2.2	Momentum Equation . . . . .	7
<b>3</b>	<b>Turbulence Modeling</b>	<b>9</b>
3.1	The $k - \varepsilon$ Turbulence Model for Shallow Water Equations . . . . .	10
<b>II</b>	<b>Numerical Algorithms</b>	<b>13</b>
<b>4</b>	<b>The Shallow Water Equations</b>	<b>13</b>
<b>5</b>	<b>The Numerical Scheme for the SWE</b>	<b>14</b>
5.1	Lagrangian Scheme for the Convective Terms . . . . .	16
5.2	Imposition of Boundary Conditions . . . . .	17
5.2.1	Open Boundaries . . . . .	17
5.2.2	Close Boundaries . . . . .	18
<b>6</b>	<b>Numerical Scheme for the <math>k - \varepsilon</math> Model</b>	<b>19</b>
<b>7</b>	<b>Transport of a Passive Tracer</b>	<b>19</b>
<b>8</b>	<b>Parallelization Strategy</b>	<b>20</b>
8.1	Mesh Partitioning . . . . .	20
8.2	Lagrangian Integration of the Convective Term . . . . .	21
8.3	Parallel Solution of the Linear System . . . . .	21
8.4	Additive Schwarz Preconditioning for the Elliptic Problem . . . . .	23
8.5	Coarse Grid Correction . . . . .	24
8.6	Parallelization of the $k - \varepsilon$ model . . . . .	25
8.7	Parallelization of the Transport of the Scalar Tracer . . . . .	26
<b>9</b>	<b>Parallelization: Implementation Details</b>	<b>26</b>
<b>10</b>	<b>Mesh Adaption</b>	<b>29</b>
10.1	Error estimate and error indicators . . . . .	30
10.2	The mesh refinement technique . . . . .	31



10.2.1	Pre-refinement and mesh enhancement . . . . .	34
<b>11</b>	<b>Test Cases</b>	<b>35</b>
11.1	Jet in a Circular Reservoir . . . . .	35
11.2	Hydraulic Jump . . . . .	35
11.3	Parallel Computation on a Complex Geometry . . . . .	38
11.4	Abrupt enlargement of a channel; the $k - \epsilon$ model . . . . .	42
11.5	Automatic Mesh Adaption: steady state case . . . . .	43
11.6	Automatic Mesh Adaption: unsteady state case . . . . .	53
<b>III</b>	<b>User Manual</b>	<b>57</b>
<b>12</b>	<b>Structure of the Code</b>	<b>57</b>
12.1	Flow Chart . . . . .	60
<b>13</b>	<b>List of the Vectors</b>	<b>60</b>
<b>14</b>	<b>Data structures</b>	<b>63</b>
<b>15</b>	<b>Sequential Input and Output</b>	<b>65</b>
15.1	Input . . . . .	65
15.2	Output . . . . .	69
<b>16</b>	<b>The Parallel Setup</b>	<b>72</b>
16.1	Partitioning the Mesh . . . . .	72
<b>17</b>	<b>The Parallel Run</b>	<b>75</b>
17.1	The Parallel Output . . . . .	75
<b>18</b>	<b>Practical Remarks</b>	<b>76</b>
18.1	Hints . . . . .	76
18.2	When Everything Else Fails... . . . .	78
<b>A</b>	<b>PVM Quick Guide</b>	<b>79</b>
A.1	Starting PVMe . . . . .	79
A.2	PVM Messages . . . . .	81



## Abstract

SWEET (**S**hallow **W**ater **E**quations **E**volving in **T**ime) is a code for the solution of the 2D de Saint Venant equations, written in their conservative form. The code adopts a Finite Differences scheme to advance in time, with a fractional step procedure. The space discretization is realized through Finite Elements, with a linear representation of the water elevation and a quadratic representation of the unit-width discharge. In this document, the physical model and the numerical schemes used for solving the resulting equations are extensively described. The accuracy of the scheme is verified in different test cases.

The sequential algorithm has been ported in the parallel computing framework by using the domain decomposition approach. The Schwarz algorithm has been added to the scheme for preconditioning the iterative solution of the elliptic equation modeling the dynamics of the elevation of the water level. The performance of the parallel code are evaluated on a large size computational test case.

The structure of the code is explained by a description of the role of each subroutine and by a flowchart of the program.

The input and output files are described in detail, as they constitute the user interface of the code. Both input and output files have a simple structure, and any effort has been made to simplify the procedure of the input setup for the parallel code, and to manage the output results.

The PVM message passing library has been used to perform the communications in the parallel version of SWEET. A short introduction to PVM is added at the end of the present report.

The SWEET package is the results of a joint work between CRS4 and Enel - Polo Idraulico e Strutturale. The authors of this document kindly acknowledge the valuable contributions of Vincenzo Pennati, from Enel - Polo Idraulico e Strutturale, and of Luca Formaggia, Alfio Quarteroni and Alan Scheinine, from CRS4.

This manual is an extension and revision of the *SWEET User Manual Version 1.0, 1996*. The author of the former document, as well as of the largest part of the SWEET code, is Davide Ambrosi, currently at Politecnico di Torino. To him, not only our sincere thank is due, but mainly the recognizance that SWEET is and will remain a work of his.



$\pi\alpha\nu\tau\alpha$   $\rho\epsilon\iota$  (Everything flows)  
*Heracitus*, *V sec. b.c.*



## Part I

# Physical Modeling

## 1 The 3D Navier–Stokes Equations

Let us consider the Reynolds–averaged incompressible Navier–Stokes (NS) equations for a free surface fluid,

$$\frac{\partial u}{\partial t} + u \frac{\partial u}{\partial x} + v \frac{\partial u}{\partial y} + w \frac{\partial u}{\partial z} - \nabla \cdot (\nu_h \nabla u) - \frac{\partial}{\partial z} \left( \nu_v \frac{\partial u}{\partial z} \right) + \frac{1}{\rho} \frac{\partial p}{\partial x} = f_v \quad (1)$$

$$\frac{\partial v}{\partial t} + u \frac{\partial v}{\partial x} + v \frac{\partial v}{\partial y} + w \frac{\partial v}{\partial z} - \nabla \cdot (\nu_h \nabla v) - \frac{\partial}{\partial z} \left( \nu_v \frac{\partial v}{\partial z} \right) + \frac{1}{\rho} \frac{\partial p}{\partial y} = -f_u \quad (2)$$

$$\frac{\partial w}{\partial t} + u \frac{\partial w}{\partial x} + v \frac{\partial w}{\partial y} + w \frac{\partial w}{\partial z} - \nabla \cdot (\nu_h \nabla w) - \frac{\partial}{\partial z} \left( \nu_v \frac{\partial w}{\partial z} \right) + \frac{1}{\rho} \frac{\partial p}{\partial z} = g \quad (3)$$

$$\frac{\partial u}{\partial x} + \frac{\partial v}{\partial y} + \frac{\partial w}{\partial z} = 0 \quad (4)$$

$$\frac{\partial T}{\partial t} + u \frac{\partial T}{\partial x} + v \frac{\partial T}{\partial y} + w \frac{\partial T}{\partial z} - \nabla \cdot (\chi_h \nabla T) - \frac{\partial}{\partial z} \left( \chi_v \frac{\partial T}{\partial z} \right) = 0 \quad (5)$$

where  $(u, v, w)^T$  is the velocity vector,  $\nu_h$  is the horizontal eddy viscosity,  $\nu_v$  is the vertical eddy viscosity,  $\rho$  is the density,  $\nabla$  and  $\nabla \cdot$  represent the horizontal gradient and the horizontal divergence respectively,  $p$  is the pressure,  $g$  is the gravity acceleration,  $T$  is the temperature,  $\chi_h$  is the horizontal eddy diffusivity and  $\chi_v$  is the vertical eddy diffusivity. The values of  $\nu_h$  and  $\nu_v$  are usually very different, due to the fact that the horizontal dimensions of the water body are often much larger than the vertical dimension. Here we neglect the internal energy transfer due to viscous effects. The fluid domain is vertically bounded by the surfaces satisfying the following equations:

$$z = \xi(x, y, t) \quad (6)$$

$$z = -h_0(x, y) \quad (7)$$

The boundary condition on the free surface is that the fluid doesn't cross it, i.e. the fluid moves with velocity equal to that of the surface itself:

$$w = \frac{\partial \xi}{\partial t} + u \frac{\partial \xi}{\partial x} + v \frac{\partial \xi}{\partial y} \quad (8)$$

At the bottom it is possible to consider free-slip or no-slip boundary conditions:



$$w = -u \frac{\partial h_0}{\partial x} - v \frac{\partial h_0}{\partial y} \quad (9)$$

$$u = v = w = 0 \quad (10)$$

In the present work we suppose that the pressure field is almost hydrostatic, i.e. that the vertical accelerations in the fluid are negligible with respect to the hydrostatic pressure gradient, so that equation (3) can be approximated as follows:

$$\frac{1}{\rho} \frac{\partial p}{\partial z} - g = 0 \quad (11)$$

The assumption (11) is valid only when the vertical accelerations are small, i.e. when the wavelength is much greater than the height of the wave itself, so that it is usually referred to these equations as *long waves* model. However, when investigating the range of applicability that this assumption allows, it is sometimes used as non-dimensional reference quantity the ratio between the basin depth and the basin width, instead of the amplitude and length of the involved waves. This implies an identification between these quantities that should be verified case by case.

## 2 Shallow Water Model

The shallow water equations (also referred to as de Saint Venant equations) are derived integrating the Navier–Stokes equations along the vertical under the hypothesis of constant density. In this way, only the average velocity is involved and a 2D description is recovered.

If  $\rho$  is constant, equation (11) is immediately integrated as follows:

$$p = p_0 + \rho g(\xi - z) \quad (12)$$

Defining

$$u_a(x, y, t) = \frac{1}{h} \int_{-h_0}^{\xi} u(x, y, z, t) dz \quad (13)$$

$$v_a(x, y, t) = \frac{1}{h} \int_{-h_0}^{\xi} v(x, y, z, t) dz \quad (14)$$

the horizontal velocities can be written as



$$u(x, y, z, t) = u_a(x, y, t) + u'(x, y, z, t) \quad (15)$$

$$v(x, y, z, t) = v_a(x, y, t) + v'(x, y, z, t) \quad (16)$$

where

$$\int_{-h_0}^{\xi} u'(x, y, z, t) dz = 0 \quad (17)$$

$$\int_{-h_0}^{\xi} v'(x, y, z, t) dz = 0 \quad (18)$$

We recall the Leibnitz differentiation rule that will be useful in the next:

$$\frac{\partial}{\partial x} \int_{b(x)}^{a(x)} f(x, y) dy = \int_{b(x)}^{a(x)} \frac{\partial f(x, y)}{\partial x} dy + f(x, a(x)) \frac{\partial a(x)}{\partial x} - f(x, b(x)) \frac{\partial b(x)}{\partial x} \quad (19)$$

## 2.1 Continuity Equation

Integration of the continuity equation along the vertical yields

$$\begin{aligned} w|_{\xi} - w|_{-h_0} &= - \int_{-h_0}^{\xi} \frac{\partial u}{\partial x} dz - \int_{-h_0}^{\xi} \frac{\partial v}{\partial y} dz \\ &= - \frac{\partial}{\partial x} \int_{-h_0}^{\xi} u dz + u|_{\xi} \frac{\partial \xi}{\partial x} - u|_{-h_0} \frac{\partial(-h_0)}{\partial x} - \frac{\partial}{\partial y} \int_{-h_0}^{\xi} v dz + v|_{\xi} \frac{\partial \xi}{\partial y} - v|_{-h_0} \frac{\partial(-h_0)}{\partial y} \end{aligned} \quad (20)$$

Using the boundary equations (8-9) and simplifying we find

$$\frac{\partial \xi}{\partial t} + \frac{\partial(hu_a)}{\partial x} + \frac{\partial(hv_a)}{\partial y} = 0 \quad (21)$$

Note that only the assumption of constant density has been used to derive expression (21).

## 2.2 Momentum Equation

We integrate the horizontal momentum NS equations along the vertical; considering each term separately, we get



$$\int_{-h_0}^{\xi} \frac{\partial u}{\partial t} dz = \frac{\partial}{\partial t} \int_{-h_0}^{\xi} u dz - u|_{\xi} \frac{\partial \xi}{\partial t} \quad (22)$$

$$\int_{-h_0}^{\xi} \frac{\partial(uu)}{\partial x} dz = \frac{\partial}{\partial x} \int_{-h_0}^{\xi} uu dz - (uu)|_{\xi} \frac{\partial \xi}{\partial x} + (uu)|_{-h_0} \frac{\partial(-h_0)}{\partial x} \quad (23)$$

$$\int_{-h_0}^{\xi} \frac{\partial(uv)}{\partial y} dz = \frac{\partial}{\partial y} \int_{-h_0}^{\xi} uv dz - (uv)|_{\xi} \frac{\partial \xi}{\partial y} + (uv)|_{-h_0} \frac{\partial(-h_0)}{\partial y} \quad (24)$$

$$\int_{-h_0}^{\xi} \frac{\partial(uw)}{\partial z} dz = (uw)|_{\xi} - (uw)|_{-h_0}. \quad (25)$$

Summing up and using the boundary conditions (8-9) these terms reduce to

$$\frac{\partial}{\partial t} \int_{-h_0}^{\xi} u dz + \frac{\partial}{\partial x} \int_{-h_0}^{\xi} uu dz + \frac{\partial}{\partial y} \int_{-h_0}^{\xi} uv dz \quad (26)$$

Introducing the unknowns defined in (15-16) we get

$$\frac{\partial}{\partial t} \int_{-h_0}^{\xi} u_a dz + \frac{\partial}{\partial x} \int_{-h_0}^{\xi} u_a u_a dz + \frac{\partial}{\partial x} \int_{-h_0}^{\xi} u' u' dz + \frac{\partial}{\partial y} \int_{-h_0}^{\xi} u_a v_a dz + \frac{\partial}{\partial y} \int_{-h_0}^{\xi} u' v' dz \quad (27)$$

To close the problem, we do the following *additional hypothesis*: the sum of the terms involving  $u', v'$  plus the vertical average of the horizontal diffusion terms in (1-2) are supposed to depend on the average velocity as follows:

$$\frac{\partial}{\partial x} \int_{-h_0}^{\xi} u' u' dz + \int_{-h_0}^{\xi} \frac{\partial}{\partial x} \left( \nu_h \frac{\partial u}{\partial x} \right) dz = \frac{\partial}{\partial x} \left( \nu_k \frac{\partial}{\partial x} (hu_a) \right) \quad (28)$$

$$\frac{\partial}{\partial y} \int_{-h_0}^{\xi} u' v' dz + \int_{-h_0}^{\xi} \frac{\partial}{\partial y} \left( \nu_h \frac{\partial u}{\partial y} \right) dz = \frac{\partial}{\partial y} \left( \nu_k \frac{\partial}{\partial y} (hu_a) \right) \quad (29)$$

where  $\nu_k$  is a parameter which should account both for turbulence and vertical dishomogeneities.

The integration of the vertical diffusion term (1-2) gives

$$\int_{-h_0}^{\xi} \frac{\partial}{\partial z} \left( \nu_v \frac{\partial u}{\partial z} \right) dz = (\nu_v \frac{\partial u}{\partial z})|_{-h_0}^{\xi} = \tau|_{\xi} + \tau|_{-h_0} \quad (30)$$

The right hand side terms are the wind stress and the bottom stress, which are usually modeled as follows:



$$\tau|_{\xi} = C_w W W_x \quad (31)$$

$$\tau|_{-h_0} = -\frac{g u_a (u_a^2 + v_a^2)^{1/2}}{K_s^2 h^{1/3}} \quad (32)$$

Repeating the same derivation for the  $y$  component and collecting the all contributions, the shallow water equations finally have the following form

$$\begin{aligned} \frac{\partial(hu_a)}{\partial t} + \frac{\partial(hu_a u_a)}{\partial x} + \frac{\partial(hu_a v_a)}{\partial y} - \nabla \cdot (\nu_h \nabla hu_a) + gh \frac{\partial \xi}{\partial x} = \\ f v_a + C_w W W_x - \frac{g u_a (u_a^2 + v_a^2)^{1/2}}{K_s^2 h^{1/3}} \end{aligned} \quad (33)$$

$$\begin{aligned} \frac{\partial(hv_a)}{\partial t} + \frac{\partial(hu_a v_a)}{\partial x} + \frac{\partial(hv_a v_a)}{\partial y} - \nabla \cdot (\nu_h \nabla hv_a) + gh \frac{\partial \xi}{\partial y} = \\ - f u_a + C_w W W_y - \frac{g v_a (u_a^2 + v_a^2)^{1/2}}{K_s^2 h^{1/3}} \end{aligned} \quad (34)$$

$$\frac{\partial \xi}{\partial t} + \frac{\partial(hu_a)}{\partial x} + \frac{\partial(hv_a)}{\partial y} = 0 \quad (35)$$

Let's use from now on a different notation, to adhere more strictly to what can be found in the source code of SWEET. Let  $\mathbf{q}(x, y, t) = (q_x, q_y)^T$  be the unit-width discharge, that is  $q_x = hu_a$ ,  $q_y = hv_a$ , and  $\mathbf{w}$  the wind stress tensor, that is  $w_x = C_w W W_x$  and  $w_y = C_w W W_y$ , with  $W = \sqrt{W_x^2 + W_y^2}$ . Then, the Shallow Water Equations, SWE from now on, read :

$$\frac{\partial \mathbf{q}}{\partial t} + \nabla \cdot (\mathbf{q} \mathbf{q} / h) - \nabla \cdot (\nu \nabla \mathbf{q}) + gh \nabla \xi = -g \frac{\mathbf{q} |\mathbf{q}|}{h^2 h^{1/3} K^2} - 2\Omega \times \mathbf{q} + \mathbf{w} \quad (36)$$

$$\frac{\partial \xi}{\partial t} + \nabla \cdot \mathbf{q} = 0 \quad (37)$$

Clearly,  $\xi$  is the elevation over a reference plane,  $h$  is the total depth of the water,  $\nu$  is the horizontal dispersion coefficient (formerly  $\nu_h$ ),  $g$  is the gravity acceleration,  $K$  is the Strickler coefficient. In the Coriolis term,  $\Omega$  is the angular velocity of the earth.

### 3 Turbulence Modeling

The Shallow Water Equations describe the motion of a turbulent flow in a satisfactory way, but in any practical numerical solution, the computational grid needed to fully resolve the turbulent motion would be too fine to fit in the memory of any computer.



Turbulent motion indeed occurs on a great range of length scale. The energy is passed from big vortices to smaller vortices, in a cascade process, and it is eventually dissipated by viscous effect at a very small scale (the turbulent scale, where all the Fourier modes are dissipated). Being impossible to describe the motion of the fluid in such detail, we are forced to resort to a modelization of the effects that the turbulent sub-grid motion has on the fluid motion which we are willing to compute on our computational mesh. A great variety of turbulence models have been proposed through the years. Here we are interested in those methods which rely upon the Eddy Viscosity/Diffusivity concept, first introduced by Boussinesq, which models turbulent stresses as proportional to the mean velocity field, introducing the concept of a turbulent viscosity, in addition to the usual physical viscosity. The values for this new viscosity can be obtained through algebraic models, or through the solution of one or two equations, which describe the temporal and spatial evolution of some quantities related to the turbulent viscosity.

We have chosen the most classical between the two-equations models, the so-called  $k - \varepsilon$  model, to be implemented in the SWEET code. This model determine the turbulent viscosity through the evaluation of two quantities, the turbulent kinetic energy  $k$  and its rate of dissipation  $\varepsilon$ . This is accomplished through the solution of two coupled advection-diffusion equations. Appropriate conditions for  $k$  and  $\varepsilon$  on closed and open boundary have to be tuned in a suitable way, as explained in the following paragraph.

### 3.1 The $k - \varepsilon$ Turbulence Model for Shallow Water Equations

We will not derived the formulation of the  $k - \varepsilon$  model for the SWE, an excellent introduction being easily found in [21].

The Reynolds averaged shallow water equations in conservative differential form read

$$\begin{aligned} \frac{\partial \mathbf{q}}{\partial t} + \nabla \cdot (\mathbf{q}\mathbf{q}/h) - \nabla \cdot \left( (\nu + \nu_t)(\nabla \mathbf{q} + \nabla \mathbf{q}^T) \right) + h \nabla \left( g\xi + \frac{2}{3}k \right) = \\ -g \frac{\mathbf{q}|\mathbf{q}|}{h^2 h^{1/3} K^2} - 2\Omega \times \mathbf{q} \end{aligned} \quad (38)$$

$$\frac{\partial \xi}{\partial t} + \nabla \cdot \mathbf{q} = 0 \quad (39)$$

where  $\mathbf{q}(x, y, t) = (q_x, q_y)^T$  is the unit-width discharge,  $\xi$  is the elevation over a reference plane,  $h$  is the total depth of the water,  $\nu$  is the kinematic viscosity (about  $10^{-6} \text{ m}^2 \text{ s}^{-1}$  for water),  $\nu_t$  is the turbulent viscosity, computed as

$$\nu_t = c_\mu \frac{k^2}{\varepsilon}$$

$g$  is the gravity acceleration,  $\Omega$  is the angular velocity of the earth,  $K$  is the Strickler coefficient.



Equation (38) is slightly different from the momentum equation (36) for laminar flow. All the differences are in the stress tensor, accounting for turbulent diffusion. It is not constant in space, has diagonal part  $\frac{2}{3}k$ , involves the operator  $\nabla \mathbf{q}^T$  coupling the two components of the momentum equation. The Reynolds stress models only turbulent diffusion and does not account for momentum dispersion due to vertical non-homogeneity of the horizontal velocities. Such aspect is not addressed here and only turbulence modeling is discussed.

The vertically averaged turbulent kinetic energy  $k$  and the rate of dissipation of turbulent kinetic energy  $\varepsilon$  obey to the following equations:

$$\frac{\partial k}{\partial t} + (\mathbf{v} \cdot \nabla)k - \nabla \cdot ((\nu + \nu_t)\nabla k) = P + P_k - \varepsilon \quad (40)$$

$$\frac{\partial \varepsilon}{\partial t} + (\mathbf{v} \cdot \nabla)\varepsilon - \nabla \cdot \left( \left( \nu + \frac{c_\varepsilon}{c_\mu} \nu_t \right) \nabla \varepsilon \right) = \frac{c_1}{c_\mu} \frac{\varepsilon}{k} P + P_\varepsilon - c_2 \frac{\varepsilon^2}{k} \quad (41)$$

where the constants  $c_\mu = 0.09, c_1 = 0.126, c_2 = 1.92, c_\varepsilon = 0.07$ , are based on classical test cases, and  $P$  is the production term, due to horizontal gradient of velocity, which expression is

$$P = \nu_t \sum_{i,j=1}^2 \frac{\partial v_i}{\partial x_j} \left( \frac{\partial v_i}{\partial x_j} + \frac{\partial v_j}{\partial x_i} \right) = \frac{\nu_t}{2} |\nabla \mathbf{v} + \nabla \mathbf{v}^T|^2$$

Equations (40-41) are different from the ones usually referred as  $k - \varepsilon$  model. The difference is in the presence of two source terms  $P_k$  and  $P_\varepsilon$ , that were first proposed by Rodi et al. [21]. These terms account for production of kinetic energy and rate of dissipation of kinetic energy due to bottom friction. The production terms  $P_k, P_\varepsilon$  are related to the vertically averaged velocity as follows:

$$P_k = c_{kp} \frac{(U^*)^3}{h} \quad (42)$$

$$P_\varepsilon = c_{\varepsilon p} \frac{(U^*)^4}{h^2} \quad (43)$$

with

$$c_{kp} = \frac{1}{\sqrt{c_f}}, \quad \text{and} \quad c_{\varepsilon p} = 3.6 \frac{c_2}{c_f^{3/4}} \sqrt{c_\mu}$$

$c_f$  is the coefficient of friction, that we have chosen to deduce from the Strickler formula

$$c_f = \frac{g}{h^{1/3} K^2}$$

and  $U^*$  is the friction velocity at the bottom equal to

$$U^* = \sqrt{c_f(u^2 + v^2)}$$



The form of the model which has been presented above is valid only for fully turbulent flows. Close to solid walls there are inevitably regions where the local Reynolds number of turbulence (measured with  $y^+$ ) is so small that viscous effects predominate over turbulent ones. A special treatment is required in order to obtain realistic numerical predictions. In SWEET the simple but efficient effective viscosity wall function approach has been taken.

Considering the existence of a local turbulence equilibrium at the solid boundary, such that production (by shear stress on the boundary and on the bottom) is equal to dissipation, the value of  $k$  and  $\varepsilon$  at a distance  $\delta$  from the solid wall are given by

$$k = c_\mu^{-1/2} u_\tau^2 + \frac{1}{3.6 c_\mu^{1/2} c_f^{1/4}} (U^*)^2 \quad (44)$$

$$\varepsilon = \frac{1}{\chi \delta} u_\tau^3 + P_k \quad (45)$$

where  $u_\tau = \sqrt{\nu \left| \frac{\partial(\mathbf{v} \cdot \boldsymbol{\tau})}{\partial n} \right|_{\text{wall}}}$  is the component parallel to the wall of the shear velocity. These boundary conditions are valid at a distance  $\delta$  from the wall such that the local Reynolds number, defined as

$$y^+ = \frac{u_\tau \delta}{\nu}$$

is such that  $y^+ \in [20, 100]$ . Following the Hinze's hypothesis, the condition for the parallel component of the velocity at the wall is

$$\mathbf{v} \cdot \boldsymbol{\tau} = u_\tau \left( \frac{1}{\chi} \log(\zeta y^+) \right) \quad (46)$$

where  $\chi = 0.41$  is the von Karman constant, and  $\zeta$  depends on the roughness of the walls (we have considered hydraulically smooth walls for which  $\zeta = 9$ ),  $n$  and  $\tau$  are the versors normal and tangent to the closed boundary, respectively.

At the open boundaries, on the contrary, where the discharge is imposed Dirichlet boundary conditions are enforced, and elsewhere natural boundary conditions have been imposed for  $k$  and  $\varepsilon$ , while the boundary conditions for  $\mathbf{q}, \xi$  are not different from the ones used for laminar flow.



## Part II

# Numerical Algorithms

## Introduction to the Numerical Discretization

The time-advancing method adopted for SWEET is of fractional step type. The main idea underlying this formulation is the splitting, at every time step, of the equations of the differential system, in order to decouple the physical contributions. In particular, the wave traveling at speed  $\sqrt{gh}$ , which is the most restrictive with respect to the maximum time-step allowed in this kind of problem, is treated implicitly with a low computational cost. In the discussion of the numerical results it will be shown that this method, coupled with a Lagrangian treatment of the convective terms, totally avoids the oscillations for the velocity that are known to plague the finite element approximations of the shallow water equations written in primitive form.[2]

## 4 The Shallow Water Equations

Let's rewrite the SWE of eqs. (34) once again:

$$\frac{\partial \mathbf{q}}{\partial t} + \nabla \cdot (\mathbf{q}\mathbf{q}/h) - \nabla \cdot (\nu \nabla \mathbf{q}) + gh \nabla \xi = -g \frac{\mathbf{q}|\mathbf{q}|}{h^2 h^{1/3} K^2} - 2\Omega \times \mathbf{q} \quad (47)$$

$$\frac{\partial \xi}{\partial t} + \nabla \cdot \mathbf{q} = 0 \quad (48)$$

As before, we have that:  $\mathbf{q}(x, y, t) = (q_x, q_y)^T$  is the unit-width discharge, that is  $q_x = hu_a$ ,  $q_y = hv_a$ ,  $\xi$  is the elevation over a reference plane,  $h$  is the total depth of the water,  $\nu$  is the horizontal dispersion coefficient,  $g$  is the gravity acceleration,  $K$  is the Strickler coefficient and  $\Omega$  is the angular velocity of the earth. A schematic representation of some of these quantities may be seen in Figure 1.

According to the theory of characteristics, if  $\nu = 0$  and the flow is subcritical, two boundary conditions are to be prescribed at the inflow and one at the outflow. However, when considering the case  $\nu \neq 0$ , the presence of the diffusion term in system (47-48) requires the imposition of a proper boundary condition for the unit-width discharge on the whole boundary and, moreover, as  $\nu$  is usually very small in the applications, it is natural to require that these boundary conditions recall the inviscid case as the viscosity coefficient tends to zero. Therefore, the boundary conditions applied here are as follows: as many Dirichlet conditions as required by the characteristic theory plus Neumann boundary conditions for each component of the unit-width discharge where its value is not yet imposed. Note that the weak Neumann condition on  $\mathbf{q}$  arises naturally in the integration by parts of the diffusive term, when considering the weak form of (47).



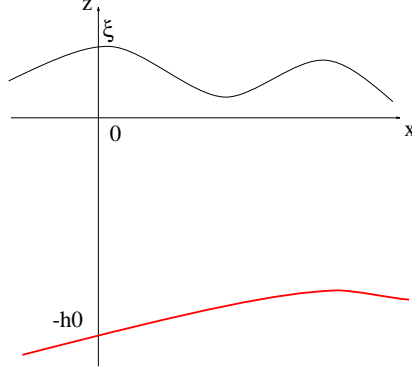


Figure 1: Elevation and depth.

## 5 The Numerical Scheme for the SWE

The main idea behind the adopted time-advancing scheme is to split the equations at every time step, in order to decouple the physical contributions. The discretization in time of the system (47-48) leads to the following equations to be solved:

Step 1

$$\mathbf{v}^n = \mathbf{q}^n / h^n, \quad \mathbf{v}^{n+1/3} = \mathbf{v}^n \circ \mathbf{X} \quad (49)$$

Step 2

$$\begin{aligned} \mathbf{q}^{n+1/3} &= h^n \mathbf{v}^{n+1/3} \\ \mathbf{q}^{n+2/3} + \Delta t g \frac{\mathbf{q}^{n+2/3} |\mathbf{q}^{n+1/3}|}{h^2 h^{1/3} K^2} &= \mathbf{q}^{n+1/3} + \Delta t \left[ \nabla \cdot (\nu \nabla \mathbf{q}^{n+1/3}) - 2\Omega \times \mathbf{q}^{n+1/3} \right] \end{aligned} \quad (50)$$

Step 3

$$\mathbf{q}^{n+1} - \mathbf{q}^{n+2/3} + \Delta t g h^n \nabla \xi^{n+1} - \frac{\mathbf{q}^{n+2/3}}{h^n} (\xi^{n+1} - \xi^n) = 0 \quad (51)$$

$$\xi^{n+1} - \xi^n + \Delta t \nabla \cdot \mathbf{q}^{n+1} = 0 \quad (52)$$

The symbol  $\mathbf{v}^n \circ \mathbf{X}$  indicates the value of the velocity, obtained by a Lagrangian integration using the method discussed in Section 5.1. At the third step, the equations (51) and (52) are decoupled by subtracting the divergence of (51) from (52). One then solves the following Helmholtz-type equation:

$$\xi^{n+1} - (\Delta t)^2 \nabla \cdot (g h^n \nabla \xi^{n+1}) + \Delta t \nabla \cdot \left( \frac{\mathbf{q}^{n+2/3}}{h^n} \xi^{n+1} \right) = \xi^n \quad (53)$$

$$-\Delta t \nabla \cdot \mathbf{q}^{n+2/3} + \Delta t \nabla \cdot \left( \frac{\mathbf{q}^{n+2/3}}{h^n} \xi^n \right) \quad (54)$$



This new elevation is then used to solve equation (51).

The spatial discretization of equations (50-52) is based on the Galerkin finite element method; the basic theory of the Galerkin approach may be found, for example, in [1], [3] and in reference [5], which treats the SWE. The weak formulation of equations (49-52), is accomplished in a standard way, and is not shown here. An important aspect of the spatial discretization of equations (50-53) is that two different spaces of representation have been used for the unknowns: the elevation is interpolated by P1 functions, whilst the unit-width discharge is interpolated by P2 functions. As usual, P1 is the set of piecewise linear functions on triangles and P2 is the set of piecewise quadratic functions on triangles. The choice of these interpolation spaces, first suggested in [4], eliminates the spurious oscillations that arise in the elevation field when a P1-P1 representation is used. To knowledge, no theoretical explanation of incompatibility between spaces of representation of the unknowns has yet been stated theoretically for the SWE.

The main advantage of this fractional step procedure is that the wave traveling at speed  $\sqrt{gh}$  is decoupled in the equations and treated implicitly. Therefore, the CFL condition due to the celerity is cheaply circumvented. Moreover, as the Lagrangian integration is unconditionally stable and all the terms appearing in eq. (50) are discretized implicitly, the resulting scheme is unconditionally stable.

A drawback of a fractional step scheme as the one adopted here is that this scheme is only first order accurate in time. However, this is not an actual disadvantage as the model deals with tidal phenomena that vary slowly in time. From a mathematical point of view, in this fractional step framework one requires, *a priori*, that the boundary conditions to be satisfied by the collection of fractional steps coincide with the boundary conditions to be satisfied by the original differential system, as described in Section 4. Unfortunately, at Step 3 the solution of the elliptic equation (53) requires the imposition of proper boundary conditions for the elevation on the whole boundary and, in the practical applications, this may not be the case. To overcome this difficulty, we relax the original requirement and at this step we impose a Neumann condition on the part of the boundary where the value of the elevation is not originally given. In the test cases one can observe that this procedure works well in practice.

In the integration of the weak formulation of eqs. (50) and (51) the lumping technique has been adopted for the mass matrices of  $\mathbf{q}$ . By the term “mass lumping” we intend the use of a low order quadrature formula for the evaluation of the integrals involving the non differential terms, yielding a diagonal stiffness mass matrix. It is well known that for P2 elements a nontrivial diagonalization has to be performed (as may be the case of P1), otherwise a singular matrix is recovered (see appendix 8 of reference [5]). This difficulty has been overcome in the following way: each triangle of the mesh is divided into four parts by connecting the midpoints of the sides; it is then possible to use the three vertex-points rule on each subtriangle. The total integral is then the sum of the subintegrals and automatically leads to a diagonal mass matrix.

A possible objection to this approach is that the mass lumping technique is known



to produce large phase errors for unsteady problems, which are precisely the ones we are interested in. However, at Step 2, no wave-type phenomena are involved and the dissipation coefficient is usually so small that the diffusive term can be treated explicitly without resulting in any additional unphysical constraints. On the other hand, when considering equation (51), for given  $\xi^{n+1}$ , the equation is explicit.

The computational effort required by this scheme for the solution of algebraic systems therefore consists of the inversion of one symmetric matrix, with size coinciding with the number of P1 nodes.

## 5.1 Lagrangian Scheme for the Convective Terms

At Step 1, the advective part of the momentum equation is integrated by a Lagrangian scheme [6, 7]. Rewriting the convective terms of equation (47) in Lagrangian form, results in the solution of two coupled ordinary differential equations:

$$\frac{d\mathbf{v}(\mathbf{X}(t), t)}{dt} = 0 \quad (55)$$

$$\frac{d\mathbf{X}}{dt} = \mathbf{v}(\mathbf{X}(t), t) \quad (56)$$

The curve  $\mathbf{X}(t)$  is the characteristic line and its slope is the velocity itself so that, at this stage, it coincides with the pathline. The velocity field plays a double role: it is the unknown to be determined as well as the slope of the characteristic curve. As we are interested in computing the solution at the nodes of the mesh, let us consider the node with coordinates  $\mathbf{y}$ . The initial condition associated with equation (56) must be:

$$\mathbf{X}(t^{n+1}) = \mathbf{y} \quad (57)$$

To integrate equation (56) we need to know the slope of the characteristic curve at  $\mathbf{y}$  at time  $t^{n+1}$  which, unfortunately, is the unknown velocity itself. Therefore, the slope of the characteristic line has to be approximated in some way, for instance by a zero-order extrapolation in time. Assuming the use of a second-order Runge-Kutta scheme to integrate equation (56), the algorithm is as follows:

$$\bar{\mathbf{X}} = \mathbf{y} - \frac{\Delta t}{2} \mathbf{v}^n(\mathbf{y}) \quad (58)$$

$$\mathbf{X}(t^n) = \mathbf{y} - \Delta t \mathbf{v}^n(\bar{\mathbf{X}}) \quad (59)$$

and equations (55) immediately give:

$$\mathbf{v}^{n+1/3}(\mathbf{y}) = \mathbf{v}(\mathbf{X}(t^{n+1}), t^{n+1}) = \mathbf{v}(\mathbf{X}(t^n), t^n) \quad (60)$$



As the Lagrangian integration requires the primitive form of the equations, the fourth term that appears in the left hand side of (51) has been added to ensure consistency with equation (47), which is written in conservative form. We note that, apart from this term, the discrete counterpart of equations (49-52) requires the inversion of symmetric matrices only. However, this consistency term is of minor relevance in all the flows in which the typical time scale is much larger than the time step (as is the case of tides). Therefore, the usual Conjugate Gradient (CG) algorithm can be confidently used in this kind of simulation.

The Lagrangian discretization of the transport terms has many attractive features: it avoids spurious oscillations arising due to the centered treatment, without the inclusion of any unphysical viscosity coefficient and it eliminates any restriction on the time step. However, when using unstructured grids the pathline reconstruction, which requires the knowledge of the element in which the foot of the pathline falls, consists of a greater algorithmic effort than that on structured grids. In practice, this difficulty has been overcome in the code by defining an ordered list containing all the elements that are adjacent to a node or to a given element. In this way the search for the element in which the pathline foot falls is restricted to clusters of elements. To avoid that the foot of the pathline reconstructed falls outside of the domain, the rigid boundary of the domain is always assumed to be a streamline.

It is worthwhile to remark that the quadratic representation of velocities, that has been adopted for compatibility reasons, fully satisfies the accuracy requirements recommended for the reconstruction of the pathline [6].

## 5.2 Imposition of Boundary Conditions

Particular conditions on the unknowns must be posed on the boundary of the integration domain. To further investigate which are the different possible conditions, we distinguish between *open* boundaries, across which we can have a net flux of water, and *closed* boundaries, i.e. solid walls.

### 5.2.1 Open Boundaries

In these regions we can impose conditions on the discharge unknown or on the elevation unknown. We can have Dirichlet b.c. on the discharge, for example at an inflow region, to impose a particular flux of water on that part of the domain, possibly changing in time. In this case, we will not have conditions on the elevation.

Alternatively we can impose Dirichlet b.c. on the elevation, for example to simulate sea tides. In this case we usually impose *natural* b.c. on the discharge, that is the requirement that the discharge must be normal to the profile of the boundary. This is done projecting the momentum equation on the normal direction.



### 5.2.2 Close Boundaries

On solid walls we can model the flow in two different ways: we can reproduce the physical situation, in which we find the water at rest, or we can ignore the friction effect of the wall, simply imposing a zero flux across the wall. The two different models are usually referred as *no-slip* and *free-slip* boundary conditions.

**No-slip boundary conditions** We impose a null velocity field all along the closed boundary, thus

$$\mathbf{q} = 0$$

on the boundary, that is we impose a Dirichlet boundary condition on the unit-width discharge.

**Free-slip boundary conditions** We ask for a null flux across the wall, by imposing a null normal component of the velocity (and thus of the discharge) along the close boundary,

$$\mathbf{q} \cdot \mathbf{n} = 0$$

where  $\mathbf{n}$  is the unit outward normal direction. As we treat the convective terms with a lagrangian procedure, we must pose this condition in a strong way. It is impossible to obtain the normal derivative in a weak form. The discretized momentum equations for the two components of the discharge give rise to two linear systems,

$$Aq_x = b_x \tag{61}$$

$$Aq_y = b_y \tag{62}$$

$$\tag{63}$$

where  $A$  is the differential operator.

Instead of the two systems above, we consider a unique system of the form :

$$\begin{pmatrix} A & 0 \\ 0 & A \end{pmatrix} \mathbf{q} = \mathbf{b} \tag{64}$$

where  $\mathbf{q} = (q_x, q_y)^T$ , and  $\mathbf{b} = (b_x, b_y)^T$ . We now couple the equations, solving on the solid boundary

$$q_x n_x + q_y n_y = 0 \tag{65}$$

and

$$A(q_x n_y - q_y n_x) = b_x n_y - b_y n_x \tag{66}$$

In the code, the first condition is imposed on the  $q_x$  variable, and the second on the  $q_y$  variable, if  $|n_x| > |n_y|$ , and the opposite is done if  $|n_y| > |n_x|$ . This procedure ensures positivity of the diagonal terms of the matrix. Please note that condition (65) imposes a null normal velocity component, while equation (66) solves the tangential component of the velocity.



## 6 Numerical Scheme for the $k - \varepsilon$ Model

The numerical approximation of the shallow water equations for turbulent flow is almost the same that was originally developed for laminar flow, and described in Section 5. We have adopted a fractional step method, where for turbulent flow it has been decided to adopt only implicit discretization because, by definition, turbulence modeling is used for flows where diffusive effects play a relevant role.

The convection of turbulent quantities is carried out by lagrangian integration, in analogy to what is done for momentum transport. The source terms are discretized implicitly or explicitly, depending on their sign. This procedure, known as semi-implicit scheme [1], reduce the cost of the fully implicit scheme; the idea is to split the terms of order zero into their positive part and negative part, and treat implicitly the positive terms and explicitly the other ones. Then all the terms on the left hand side are positive and so are all the terms on the right hand side. The maximum principle for PDE in the discrete case insures positive value of  $k$  and  $\varepsilon$ . (For physical and mathematical reasons it is essential that the system of PDE yields positive values for  $k$  and  $\varepsilon$ ).

The final scheme for the equations (3) and (4) is then

$$k^{n+1} \left( 1 + \Delta t \frac{\varepsilon^n}{k^n} \right) - \Delta t \nabla \cdot \left( (\nu + \nu_t^n) \nabla k^{n+1} \right) = k^n(X) + \Delta t P^n + \Delta t P_k^n \quad (67)$$

$$\varepsilon^{n+1} \left( 1 + \Delta t c_2 \frac{\varepsilon^n}{k^n} \right) - \Delta t \nabla \cdot \left( \left( \nu + \frac{c_\varepsilon}{c_\mu} \right) \nabla \varepsilon^{n+1} \right) = \varepsilon^n(X) + \Delta t \frac{c_1}{c_\mu} \frac{\varepsilon^n}{k^n} P^n + \Delta t P_\varepsilon^n \quad (68)$$

with

$$\nu_t^n = c_\mu \frac{(k^n)^2}{\varepsilon^n}$$

## 7 Transport of a Passive Tracer

A passive tracer is a quantity that is transported by the velocity field of the fluid, but that does not affect the fluid motion itself. It can represent a concentration of a pollutant, or a thermal field (where the effects due to the variation of density are neglected). The equation describing the evolution of the tracer is thus of the form advection-diffusion, with the possible presence of source terms:

$$\frac{\partial T}{\partial t} + \mathbf{u} \cdot \nabla T - \frac{1}{h} \nabla \cdot (h \nu_t \nabla T) = S_T \quad (69)$$

where  $T$  is the vertically integrated value of the tracer,  $\mathbf{u} = (u, v)$  is the velocity field of the fluid,  $h$  is the water depth,  $\nu_T$  is the diffusion coefficient of the tracer and  $S_T$  is the source term.



This equation is solved in SWEET through the usual algorithms used for the other equations, that is a lagrangian integration for the advective term and an implicit formulation for the diffusive term, giving rise to a linear system, solved through a conjugate gradient algorithm.

Boundary conditions are imposed only on open boundaries, where the water enters or leaves the domain. At the inlet, we impose a Dirichlet condition on  $T$ , assigning it a given value (usually zero). At the outlet, we impose the value resulting from the integration of the advective term.

## 8 Parallelization Strategy

In the numerical scheme described above, two “computational kernels” can be recognized. For equations (50-52), since all terms but  $\mathbf{q}^{n+2/3}$  are evaluated at previous time levels, the finite element formulation of equation (50) gives

$$M\mathbf{q}^{n+2/3} = \mathbf{g} \quad (70)$$

where  $\mathbf{g}$  is a known vector and  $M$  is the finite element mass matrix, i.e.

$$M_{ij} = \int_{\Omega} \phi_i \phi_j d\Omega \quad (71)$$

$\{\phi_i\}$  being the set of nodal shape functions which provide a basis of piecewise linear polynomials. By adopting a mass lumping technique [3], the solution of the Step 2 is explicit and therefore the main computational effort reduces to the following tasks:

1. Lagrangian integration of the convective term as defined by equations (55-56).
2. Solution of the elliptic problem defined by equation (53).

### 8.1 Mesh Partitioning

The strategy devised for the parallelization of the above listed computational kernels is based on domain decomposition. This technique exploits the topology of the problem, partitioning the computational domain into subregions. The fact that we are dealing with unstructured meshes poses some additional problems for the implementation of the parallel algorithms, both for defining properly the decomposition into sub-domains and for the definition of an efficient communication scheme. However, the flexibility ensured by unstructured grids is a remarkable advantage of the finite element technique when dealing with complex geometries (as it is often the case in environmental flows) and it makes the effort worthwhile.

The first step for a domain decomposition approach is the partition of the computational domain into a given number of sub-domains. The specifications characterizing such partitioning should be:



1. Minimization of the number of neighbors for each sub-domain.
2. Minimization of the number of nodal values at interfaces between sub-domains.
3. Balancing the size (i.e. the number of nodes) of each sub-domain; this will result in a balancing of the computational load between the different processors.

To perform the partitioning we have tested three software packages, Metis [11], Chaco [9] and TopDomDec [10], which implement several algorithms. The interested reader may consult the given bibliography for details. Our parallel procedure requires that the sub-domains partially overlap each other. This feature has been obtained by developing an *ad-hoc* software.

## 8.2 Lagrangian Integration of the Convective Term

The Lagrangian integration of the convective term requires the calculation of the pathlines and the evaluation of the velocity where the pathline falls. On an unstructured grid the major computational cost consists in recognizing which elements are crossed by the pathline. In practice, this operation requires, for each node and at each integration step, the computation of the area of some triangles for each mesh node. This formulation for the Lagrangian integration of the convective term does not require any matrix inversion. It is then a *local* operation, which needs for each node some information about the old solution in a cluster of elements around it.

The Lagrangian integration of the convective terms can naturally be performed in parallel in a domain decomposition framework. Each processor carries out the integration in the nodes belonging to the sub-domain assigned to the processor itself. As the pathline can exit the sub-domain, care must be used when dealing with the nodes posed in proximity of its boundary. The Lagrangian integration of the nodes belonging to the overlap region must be computed by the processor which succeeds in the reconstruction of the pathline. With regard to the nodes in the proximity of the overlap, a limit on the time step is dictated by the requirement that their pathline does not exit the sub-domain to which they belong. This means in practice that the CFL velocity number should be smaller than 2:

$$\max_{\Omega} \left( \frac{|\mathbf{v}|}{\Delta x} \right) \Delta t \leq 2 \quad (72)$$

Such a condition is not restrictive in practical applications, where the wave celerity is usually much larger than the fluid speed.

## 8.3 Parallel Solution of the Linear System

Equation (53) can be seen as a particular case of elliptic differential problem of the form:



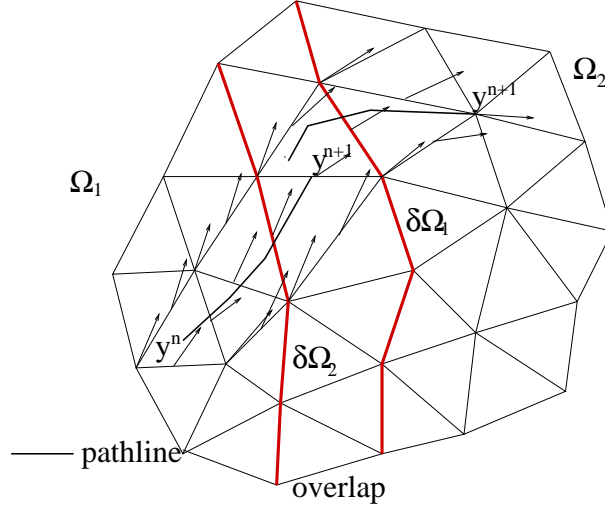


Figure 2: Lagrangian integration at the boundary between sub-domains.

$$Lu = f, \quad (73)$$

where  $u = \xi^{n+1}$ ,  $L = L(\xi^n, H, \mathbf{q}^{n+2/3}, \Delta t)$  indicates a quasi-symmetric linear operator and  $f = f(\xi^n, H, \mathbf{q}^{n+2/3}, \Delta t)$ .

After being approximated by finite elements, relation (73) can be written in the algebraic form:

$$Ax = b \quad (74)$$

The matrix  $A$  is symmetric, positive definite, sparse and, typically, very large. An effective algorithm to solve the linear problem (74) is the conjugate gradient (CG), when coupled with a suitable preconditioner.

We use a parallel implementation of a CG to solve equation (74) on a distributed memory machine. An effective parallelization of this iterative method can be obtained as follows. Let us suppose that the computational domain  $\Omega$  is partitioned into  $N$  sub-domains  $\Omega_i$ , with an overlap of one element, such that  $\Omega = \bigcup_i \Omega_i$ . We assign at every processor the job of performing the computations on the elements of the matrix belonging to a sub-domain  $\Omega_i$ . The following pseudo-code focuses the communications needed in the parallel version of the algorithm, see for instance [15].

$$r_0 := b - Ax_0, p_0 = r_0$$

For  $j = 1, \dots$  until convergence



```

 $\alpha_j = (r_j, r_j) / (Ap_j, p_j)$       inter-processor communication!
 $x_{j+1} = x_j + \alpha_j p_j$ 
 $r_{j+1} = r_j - \alpha_j Ap_j$ 
 $\beta_j = (r_{j+1}, r_{j+1}) / (r_j, r_j)$       inter-processor communication!
 $p_{j+1} = r_{j+1} + \beta_j p_j$ 
end do

```

A look at the algorithm listed above shows that the iterative method can be parallelized by exchanging information only when global scalar quantities are computed; this occurs twice in each iteration.

An efficient implementation of a standard preconditioner is not straightforward. In fact, neglecting the trivial case of diagonal preconditioning, effective techniques such as incomplete LU decomposition are intrinsically sequential. We can indeed say that the main effort in finding an efficient parallel iterative solver has to be spent in devising the appropriate preconditioner.

## 8.4 Additive Schwarz Preconditioning for the Elliptic Problem

In what follows, we briefly outline the additive Schwarz preconditioner, more details on the theory being available, as example, in Ref. [12]. The method of Schwarz has been originally proposed as a *solver*. The underlying idea is to solve the elliptic problem separately on some portions of the original integration domain, exchange information at the borders of the different portions, and then iterate the procedure till convergence, obtaining, from the union of the solutions on sub-domains, the global, exact solution of the original problem. In recent years this view of the Schwarz method as a *solver* has been practically abandoned, whereas its attractive features as a *preconditioner* have been exploited. We define  $R_i$  as the restriction operator relative to the sub-domain  $\Omega_i$  and  $A_i = R_i A R_i^T$ . Note that, from a functional point of view,  $A_i$  is the local stiffness matrix in  $\Omega_i$  as arises when imposing homogeneous Dirichlet boundary conditions on  $\partial\Omega_i$ . If we consider

$$M^{-1} = \sum_i R_i^T A_i^{-1} R_i \quad \text{where} \quad A_i = R_i A R_i^T \quad (75)$$

the parallel conjugate gradient algorithm preconditioned with the Additive Schwarz method then reads:

$$r_0 := b - Ax_0, z_0 = M^{-1}r_0, p_0 = z_0$$



For  $j = 1, \dots$  until convergence

$$\alpha_j = (r_j, z_j) / (Ap_j, p_j) \quad \text{inter-process communication!}$$

$$x_{j+1} = x_j + \alpha_j p_j$$

$$r_{j+1} = r_j - \alpha_j Ap_j$$

$$z_{j+1} = M^{-1} r_{j+1}$$

$$\beta_j = (r_{j+1}, z_{j+1}) / (r_j, z_j) \quad \text{inter-process communication!}$$

$$p_{j+1} = z_{j+1} + \beta_j p_j$$

end do

The Schwarz preconditioner is an attractive choice for parallel computations because of its locality: it does not require any exchange of information between sub-domains. Moreover, because of the definition of the restriction operator  $R_i$ , the elements of the matrix  $M$  are identical to the ones that are in the matrix  $A$ , so that no specific storage is required for the preconditioner. Finally, it may be noted that the local subproblems to be solved at the preconditioning level are always well posed because they can be seen, at a *functional* level, as the discretization of a Poisson problem with homogeneous Dirichlet boundary conditions.

An open question refers to the possibility of solving the local problems (i.e. the Schwarz preconditioning) in an approximate way. We will discuss further this subject in Section 9.

## 8.5 Coarse Grid Correction

Some theoretical results are available from the analysis of the Schwarz preconditioner. When using a regular grid of spatial step  $\Delta x$ , partitioned into sub-domains of linear length  $H$ , with overlap size  $\delta = \beta H$ , it may be shown [8, 12] that the condition number of the matrix  $M^{-1}A$  is bounded as

$$\text{cond}(M^{-1}A) \leq CL^{-2}(1 + \beta^{-2}) \quad (76)$$

where  $C$  is a value independent from  $H$  and  $\delta$ . In 2D problems,  $H^{-2}$  is proportional to the number of sub-domains, and therefore this estimate reveals a deterioration of the quality of the algorithm with the increase of the number of sub-domains. This inconvenience can be removed by introducing a *coarse grid* operator. Let's  $A_H$  be the matrix arising from the discretization of the elliptic problem on a coarse grid, whose element size is of the same order of magnitude of the sub-domains. Then we can replace  $M$  by  $M_c$ , defined as



$$M_c^{-1} = R_H^T A_H^{-1} R_H + M^{-1} \quad (77)$$

Here,  $R_H^T$  is the prolongation map from coarse to fine grid, given, for example, by a piecewise linear interpolant from coarse grid nodes. It can be shown that

$$\text{cond}(M_c^{-1} A) \leq C(1 + \beta^{-1}) \quad (78)$$

where, again,  $C$  is independent from  $H$  and  $\delta$ . Thus, the preconditioning property of the operator  $M_c$  does not depend on the number of sub-domains, but only on the amount of the overlap between them.

The coarsening of an unstructured grid can be a non-trivial task. Therefore, we have investigated a different procedure for the construction of the coarse grid operator  $A_H$ , by resorting to an agglomeration technique similar to that introduced in [13, 14] in the context of multigrid procedures. We consider  $R_H$  so that

$$A_H = R_H A R_H^T \quad (79)$$

where

$$R_{H_{ij}} = \begin{cases} 1 & \text{if } j \in \Omega_i \cup \partial\Omega \\ 0 & \text{otherwise} \end{cases}$$

The construction of  $A_H$  is thus a completely algebraic procedure and it does not require to build a coarse triangulation. There are no theoretical results concerning this operator. We have therefore resorted to numerical investigations to test its effectiveness; in Section 11.3 some computational results are shown and the performance of this algebraic coarse grid operator is discussed.

After these details, it is clear that the choice of this Schwarz preconditioner has been guided by its intrinsic parallelism and its ability to ensure, when the coarse grid correction is used, a behavior independent on the number of sub-domains, and thus on the number of processors, used in the calculation.

## 8.6 Parallelization of the $k - \varepsilon$ model

As explained in Section 6, the equations for the  $k$  and  $\varepsilon$  quantities are solved using the same numerical methods for the integration of the advective and diffusive terms of the equation for the momentum, that is a lagrangian integration for the advective terms and a conjugate gradient to solve the linear system arising from a semi-implicit formulation of the diffusive term. Thus, no new algorithm are introduced in the code, and the parallelization of the  $k - \varepsilon$  model follows the same strategy stated above.



## 8.7 Parallelization of the Transport of the Scalar Tracer

Exactly the same considerations given above hold for the advection-diffusion equation for the passive tracer.

## 9 Parallelization: Implementation Details

Even if the sub-domains overlap each other there is only one sub-domain where a given node  $i$  is considered as interior. This sub-domain will be termed as the *parent* sub-domain for that node.

The domain decomposition approach can be easily applied to the explicit parts of algorithms, since the operations are mainly local. The nodes at the boundary between sub-domains must be updated at the end of each step, by receiving the values from their parent sub-domains. Thus, lists of *sending* and *receiving* nodes are defined for every sub-domain, together with a communication pattern able to guarantee no-blocking communications.

During the Lagrangian step (Step 1), the situation is complicated by the fact that for a border node it is possible that the pathline falls outside the sub-domain. Thanks to the overlap, it is possible to perform the Lagrangian integration in the neighboring sub-domain. However, the list of the border nodes for which the pathline falls outside the sub-domain can change at each temporal iteration, depending on the velocity direction. A dynamic mechanism has then been devised for the definition of the sending and receiving nodes.

The integration of the implicit equation for the elevation at Step 3 poses different problems from the point of view of the parallel implementation of the algorithm. The CG is parallelized in a genuine domain decomposition way: the matrix, the right hand side and the unknown vector are distributed among the processors, and the matrix-times-vector and vector-times-vector operations are performed in parallel on the distributed set of data. Again, the communication scheme has been designed to avoid blocking patterns. The interprocessor communications doesn't make any use of pre-defined collective message-passing instructions, but only the base instructions `send` and `recv` of the PVM [17] message passing library. In this way the code portability is assured and its performance is reproducible.

As discussed in the previous Section, the CG is preconditioned by an additive Schwarz algorithm. To exploit all its capabilities, we decided to have the number of sub-domains for the Schwarz algorithm be independent from the number of processors. We have thus introduced a second level of subdivision into domains, so that several sub-domains can be assigned to a single processor. We first partition the domain into a number of portions  $N_p$  equal to the number of processors, then each portion is further subdivided into the final sub-domain pattern. A schematic representation of this two levels partition is presented in Figure 3.



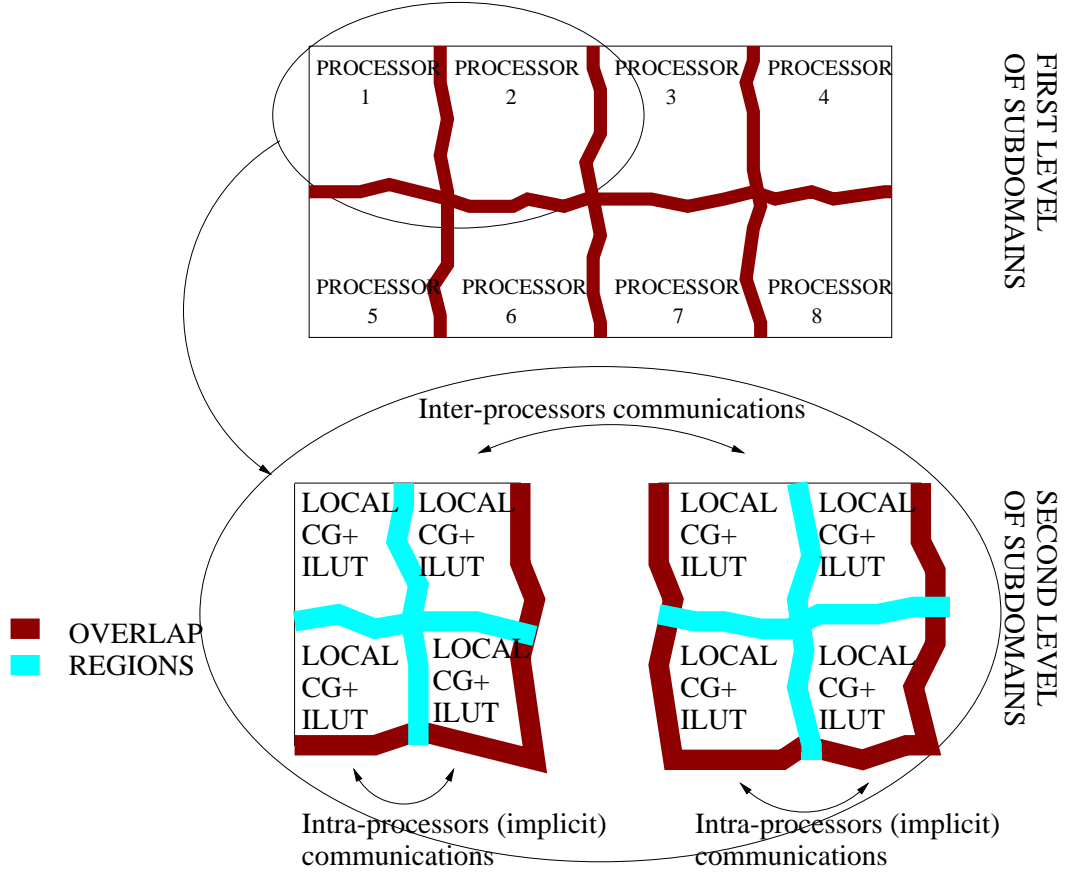


Figure 3: The two level of partitions used in the code: we imagine a run over eight processors, and thus a first level partition of the global domain in eight sub-domains. The detail on the two first sub-domains shows how every sub-domain is further partitioned in several regions. All the explicit integrations act on the first level of sub-domains. The Schwarz algorithm acts locally on the second level of sub-domains. The global CG uses the same data sets of the Schwarz algorithm. In dark grey the overlap regions for the first-level sub-domains, in light grey the overlap regions for the second-level sub-domains.



Using a large number of sub-domains for the Schwarz algorithm may produce a considerable reduction of computational time. In fact, the solution of many small linear systems can be faster than the solution of few linear systems of larger dimension. The distribution of the matrix and vectors for the global CG is made at the second level of sub-domains: in this way the same data structures are used for carrying out both the global CG and the Schwarz preconditioning, thus optimizing the memory requirements. This choice greatly complicates the managing of the communications for the global CG. To gain the maximum efficiency, we have set up a scheme that uses implicit communications via `common` blocks when the two communicating sub-domains reside on the same processor, and explicit message-passing instructions when the communication involves two different processors. Moreover, to minimize the latency time, all the messages from sub-domains residing on one processor, that are to be delivered to sub-domains all residing on another processor, are first collected in a buffer and then sent with a unique `send` instruction.

The linear systems local to the sub-domains resulting from the Schwarz algorithm are governed by the matrix  $A_i$ , which is positive definite. Therefore, we have decided to use again a CG procedure, preconditioned with an incomplete LU decomposition (ILUT)[15], for their solution. On the contrary, the coarse grid system is always solved “exactly”, by inverting the matrix  $A_H$ . We will refer to the CG iterations at sub-domain level used to solve the Schwarz preconditioning system as the “local” CG.

Since the local CG has to work just as a preconditioner, the solution of the subsystems would preferably be carried out with a low degree of accuracy. This would correspond to use an approximation of the preconditioning system. In practice, however, we have noted that the convergence rate of the global CG is heavily dependent on the accuracy of the local solutions. We thus have coupled the convergence thresholds of the local and the global CG’s so that the values of the local residuals are always lower than the current value of the global CG residual. In this way we have obtained a good overall convergence rate.

The pseudo-code of the parallel shallow water model thus reads as follows:

```

do i = 1, number of time steps

    solve Lagrangian transport in each of the  $N_p$  sub-domains
    exchange boundary conditions among the  $N_p$  sub-domains

    solve Step 2 in each of the  $N_p$  sub-domains
    exchange boundary conditions among the  $N_p$  sub-domains

do until convergence
    precondition solving local linear systems on each of the  $N_s$  sub-domains
        by CG + ILUT
    perform one CG iteration on the global domain (in parallel)

```



```

end do

solve Step 3 for the unknown  $\mathbf{q}$  in each of the  $N_p$  sub-domains
exchange boundary conditions among the  $N_p$  sub-domains

end do

```

## 10 Mesh Adaption

The use of unstructured grids for the numerical approximation of partial differential equations of applied mathematics has two great attractives. The one most commonly claimed is the geometrical flexibility, that is the capability to handle computational domains with complicated boundaries of problems that would be almost impossible to solve by a structured approach. However, there is a second aspect of unstructured grids that has even more relevance: the possibility to refine the computational mesh where needed, in order to minimize the computational error in some proper sense. Suitable indicators of the accuracy of the solution allow to refine the mesh where the numerical error is large and to coarsen it where the error is small, in order to optimize the quality of the computed solution for a given computational effort. [22]

Mesh adaption techniques have been used since many years ago in several fields of computational fluid dynamics, but adaptivity has not yet much explored in the framework of free surface hydrostatic flow. At our knowledge only a very recent paper [23] compares and discusses the use of high order polynomial basis ( $p$  adaption) for discretization of the shallow water equations versus local mesh refinement, where the the order of the polynomial approximation is kept unchanged ( $h$  adaption).

The mesh adaption technique adopted, (see section 10.2) is based on the use of a background grid (see for example [24], [25]). The numerical simulation starts on a grid, possibly composed by few nodes, which is the coarsest mesh used in the computation: its nodes are neither moved nor suppressed. Successive levels of refinement and coarsening lie on the background grid. This technique has been adopted because of the very complicated geometry of the boundary that characterizes environmental applications in river, coastal areas and so on. By keeping a background grid, the information about the position of the boundaries and bathymetry can be preserved and is not lost by further interpolations due to node movements. Remarkably, a relevant by-product of the mesh adaption is that poor care has to be used in defining the initial grid: "with adaption, any initial grid will be transformed into a near optimal discretization". [26]

A peculiar aspect of the mesh adaption for shallow water flow is the necessity to devise proper indicators of the numerical error that should drive the grid refinement and de-refinement. In the present paper three possibilities are proposed and investigated: the second order derivative of the elevation field, the second order derivative of the magnitude of the velocity and the local mass conservation in a specific sense. Every error indicator has



a mathematical basis or is suggested by numerical or physical reasons. The performance of these error estimators is discussed together with the numerical results in the last section of the paper.

## 10.1 Error estimate and error indicators

The mesh adaption technique requires some *a posteriori* estimate of the error of the numerical solution based on the computed solution itself: it is necessary to state locally how much the numerical solution differs, in a proper sense, from the exact solution of the differential problem. In this section we propose a few ways to determine where the computational mesh should be refined or coarsened.

**1.** For linear elliptic problems it is possible to estimate rigorously the numerical error in terms of the second derivative of the exact solution. Let  $u$  be the exact solution of the elliptic problem :  $\nabla u = v$ ; that is, in weak form

$$(\nabla u, \nabla v) = (b, v) \quad (80)$$

for all  $v$  belonging to a suitable space and where  $(, )$  indicates the usual internal product in  $L^2$ . Then, given a triangulation with maximum side length  $h$ , it can be shown [27] that the distance between the exact and the computed solution linear  $u_h$  in  $H^1$  is bounded as follows:

$$(\nabla(u - u_h), \nabla(u - u_h)) = \|\nabla(u - u_h)\|_{L^2}^2 \leq h^2 \max_{ij} \left| \frac{u}{x_i x_j} \right| \quad (81)$$

As the computational kernel of the numerical scheme adopted in section 4 is an elliptic equation for the elevation of the water  $\xi$ , in the refining-coarsening stage we can use the estimate (81), where the right hand side has to be calculated using the computed solution  $u_h$ . The error estimate (81) suggests to define the following non-dimensional error indicator:

$$\epsilon_{1,m} = \frac{h_m}{\xi_m} \max_{ij} \left| \sum_k \xi_k \int_{\Omega} \frac{\phi_k}{x_i} \frac{\phi_m}{x_j} d\Omega \right| \quad (82)$$

where  $\Omega$  is the computational domain and  $\phi_k$  is the  $k$ -th linear basis function.

**2.** From a more physical point of view, considering the whole shallow water equations system, it can be foreseen that there are typical behaviors of the flowfield that the error indicator  $\epsilon_1$  could not be able to detect properly. For instance, shear layers between



parallel velocities, as may happen at inflow of branches into a channel, could not be detected by the indicator (82). To this aim, it would be more useful to use an indicator of the gradients of the solution depending on the velocity magnitude. Extending in a heuristic way the definition (82) to the velocity field, we propose

$$\epsilon_{2,m} = \max_{ij} \left| \sum_k v_k \int_{\Omega} \frac{\phi_k}{x_i} \frac{\phi_m}{x_j} d\Omega \right| \quad (83)$$

where  $v$  is the magnitude of the velocity  $\mathbf{v}$ .

**3.** An important feature that a numerical scheme for shallow water flow should possess is mass conservation. This property is accomplished by the scheme described above, as the discrete equations are obtained from the continuity equations, and are then consistent with it. However, the finite element scheme illustrated above does not ensure mass conservation in a *finite-volume cell-centered* sense: the mass variation inside a triangle during a time step is not exactly equal to the flux through the edges of the triangle itself. The reason of this is twofold. On one hand the use of quadratic polynomials to approximate the discharge  $\mathbf{q}$  yields to larger computational stencil than when using a linear representation. Mass conservation checking must be done on a stencil consistent with the stencil of the scheme. The mass conservation, triangle by triangle, can be properly advocated only for finite elements of mixed type, when a special mass lumping is used. In fact, finite elements of mixed type RT0 just recover the cell-centered finite volume technique [28].

Secondly, we observe that the substitution of the momentum equation into the continuity equation, that leads to eq.(53) involves a new spatial derivation. This is a usual approach in the finite elements context [29], but does ensure local mass conservation. Conversely, in the finite difference-finite volumes framework, such a substitution is usually carried out at an algebraic level: equations (51-52) are first discretized in space and then the substitution is carried out, without further derivatives. This ensures local triangle-by-triangle mass conservation [30].

The considerations above suggest to use the check of local mass balance as an error indicator for the present scheme. We define then

$$\epsilon_{3,e} = \left| \frac{1}{\Delta t} \int_e (\xi^n - \xi^{n-1}) d\Omega + \oint_e \mathbf{q} \cdot d\mathbf{\Gamma} \right| \quad (84)$$

Here  $\mathbf{\Gamma}$  is the contour of the  $e$ -th element and  $\epsilon_{3,e}$  is the mass defect in the  $e$ -th element.

## 10.2 The mesh refinement technique

Any error estimator among the ones described in the section above allows to identify a set of elements of the mesh to be refined (or coarsened). Several techniques can be used



to this aim [26].

- 1. Repositioning of the mesh (r-methods):** local refinement of the mesh is obtained moving nodes, in order to minimize the distribution function of the error. Of course, this local refinement generates de-refinement in the remaining part of the domain. Since topology of the mesh does not change during repositioning, this strategy is easy and cheap to implement: the connectivity of the grid is unchanged. Nevertheless it is a strategy not often used, because of the constrain of using a fixed number of elements.
- 2. Enrichment of the mesh (h-methods):** the triangles of the grid are divided in elements of lower average side length  $h$ . As the error of the numerical solution behaves like  $ch^\lambda$ , with  $c$  and  $\lambda$  constants, these methods, if used in a proper way, ensure  $\lambda$ -power convergence. For this reason h-methods are most popular. although their implementation is more complex because, at every subdivision, the topology of the mesh changes. The splitting of the elements can be made essentially in two ways:
  1. edge bisection: midpoint of an edge marked to be refined is joined with the vertex opposite to this edge.
  2. standard refinement: a marked triangle (*father*) is subdivided into four similar triangles (*sons*) joining midpoints of the edges of the father. The number of edges and triangles increases for a factor four and the local length of triangles is halved.
- 3. Re-meshing (m-methods):** to produce a highest quality triangulation, creation, destruction and repositioning of the nodes is allowed. This is a more general procedure but also heavier from a computational point of view.

The choice of the more suitable mesh adaption procedure depends on the problem at the hand. For example, regularity of the element size length and shape can be a requirement or not. In compressible flow simulations, very stretched elements are useful, because where shocks are located, the flow direction is strongly biased. Adapted grids for these problems are in general very irregular both in side length and in shape ([22]). The more appropriate strategy for these kind of problems seems to be the h-method 2.1.

In the present paper we chosed to use the refinement technique 2.2 of the h-method. Main reason for this choice is that the h-methods keep the information on the original grid unchanged. When a new node is added in the middle of an edge, bathymetry, velocity and water elevation in it are obtained by interpolating the values in the element. In this way the original values of the bathymetry and of the physical unknowns in the initial mesh are never abandoned and the degradation of the solution due to the interpolation is minimized.



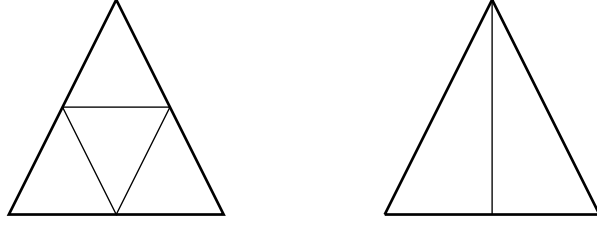


Figure 4: Red Refinement (standard or regular) and green of a triangle.

Moreover, when simulating subcritical shallow water flow, regions are more suitable to be refined instead of lines (see results in section 11.5). So, in the present work the computations are started on a mesh as regular as possible, then refinements and de-refinements are accomplished in such a way to preserve regularity.

In Figure 4 is shown the subdivision technique known as *standard* or *regular* or *red refinement* [31]. The marked elements are first divided in standard way. The surrounding triangles have then one, two or three edges sub-divided. The nodes in the midpoint of the edges of the elements not yet refined are called “hanging nodes”. Elements having *hanging nodes* must be refined in a proper way to ensure consistency of the triangulation. Among the possible strategies, we have chose the one described in the following, in C-like form:

```

for (i=0;i<NEL;i++)
    if(Err(i)>thresh) StandRef(i);
for (i=0;i<NEL;i++)
    if((NHang(i)>1) || (NHang(i)==1 EType(i)==green)) StandRef(i);
if StandRef has been called at least one time in the last block then
    it is re-executed;
for (i=0;i<NEL;i++)
    if(NHang(i)==1) MakeGreen(i);

```

`Err(i)` is a function evaluating the error on the triangle `i` with one of the described methods. `StandRef(i)` refines the triangle `i` in standard way; if the triangle is “green”, it and the sibling are substituted by the father before refinement. When executing first for-block only elements which have an error greater than a fixed error threshold `thresh` are refined. `NHang(i)` and `EType(i)` are functions which respectively return number of hanging nodes and type (standard or green) of the triangle `i`. In the second for-block triangles which have more then one, or green ones which have at least one hanging node are standard refined. If some element has been refined maybe some other hanging node has been created and for this reason this last block is re-executed till possible. In the last block `MakeGreen` green-refines triangles which have an hanging node, to ensure consistency



of the mesh.

This algorithm converges in a finite number of iterations; at most all the elements of the initial grid will be standard refined. The grid refined with the algorithm listed above has a minimum number of green elements, which are the elements deteriorating the quality of the initial mesh.

### 10.2.1 Pre-refinement and mesh enhancement

If some of the characteristics of the solution of a given problem is known a-priori it is possible, in principle, to decide some sort of pre-refinement of the mesh. For this reason a package named *prerefine* has been prepared which read the initial mesh (in SWEET format) and a vector of integers containing flags to the elements to be refined and re-write a file (in the same format) with the new mesh pre-refined.

As already mentioned, the refinement technique here adopted, generates at the boundaries of a refined area elements of poor quality. When pre-refining the initial mesh such drawback can be avoided improving the overall mesh quality by means of an algorithm known as “Laplacian smoothing”.

Given a generic node *P* of the mesh not in the boundary, we will call patch around *P* the polygon formed by all the elements which have this point in common. The information about elements which constitute the patch is contained in the structure *VVER* (see section 14. Smoothing of Laplace consists in moving every internal point of the triangulation to the baricentrum of the patch around this point. This can be done without problems when the patch is convex. When instead the patch is concave the algorithm must be modified in order to avoid that the node movement would produce an inconsistent triangulation. The modified Laplace Smoothing used in the pre-refine module is described in detail in [32].

### Refining and coarsening

When designing a practical strategy of mesh refinement-coarsening, it would be very useful to state first an acceptable numerical error and then use it as a yardstick: coarsen the mesh where the error indicator is lower than the reference one, refine when larger. Unfortunately, the error indicators described above only give, at best, estimates of the numerical error, or hints about *where* the error is larger: they do not ensure any absolute evaluation of its magnitude.

When computing steady flows, this difficulty is overcome stating first the computational resource that can be addressed, that is the maximum number of nodes to be used in the numerical simulation. Then, starting with a quite coarse mesh, it is refined until that the desired number of nodes is reached.

When dealing with unsteady flow, also coarsening is useful. In this paper we are addressing smooth flow, that is subcritical shallow water flow or, at most, locally transcritical flow. In such regime there are no discontinuities in the physical variables and, typically, the



time-dependency is due to the change of boundary conditions which is smooth in time and has a period of 12-24 hours. As time goes by, the flowfield changes and a proper mesh adaption strategy should modify the mesh, refining it in a optimal way with respect to the adopted error indicator. In this framework, instead of keeping constant the number of nodes, as was the case of steady flow, it is more significative to keep constant the maximum error indicator of the grid at any time. This ensure a constant control of the error all along the simulation.

## 11 Test Cases

To validate the numerical scheme and its sequential and parallel implementation, we consider different examples. The first two test problems have been specifically designed to test the discretization of the nonlinear terms in the equations and the mass-conservation property of the numerical scheme. In addition, they are used to test for the presence of spurious oscillations arising due to the boundary conditions. The third example is a demonstration of the parallel performance of the code.

### 11.1 Jet in a Circular Reservoir

The first problem is the simulation of a steady jet in a circular reservoir; the details of this classical test case as well as the experimental results can be found in [19]. The geometry of the boundary and the computational grid are shown in Figure 5. We use an eddy coefficient  $\nu = 2.5 \cdot 10^{-4} \text{m}^2/\text{s}$  and a time step of 2 s. The computed velocity field is shown in Figure 6. The solution does not differ much from the one shown in [6] and [19]; the location of the gyre centers are sufficiently well described, but the maximum computed velocities in the gyres are underestimated, mainly in the region near the inflow. Such a discrepancy is due to three-dimensional effects, and not to the staircase boundary that characterizes the finite difference contours used in the cited references.

### 11.2 Hydraulic Jump

The second test case that we consider is the steady 1D flow in a prismatic channel, without diffusion and bottom friction effects. Under these hypotheses the SWE reduce to

$$\mathbf{q} = (Q, 0) \quad h = h(x) \quad (85)$$

$$\frac{d}{dx} \left( \frac{Q^2}{h} \right) + gh \frac{dh}{dx} = gh \frac{dh_0}{dx} \quad (86)$$

where  $Q$  is the (constant) unit-width discharge. If the bottom field is defined as:



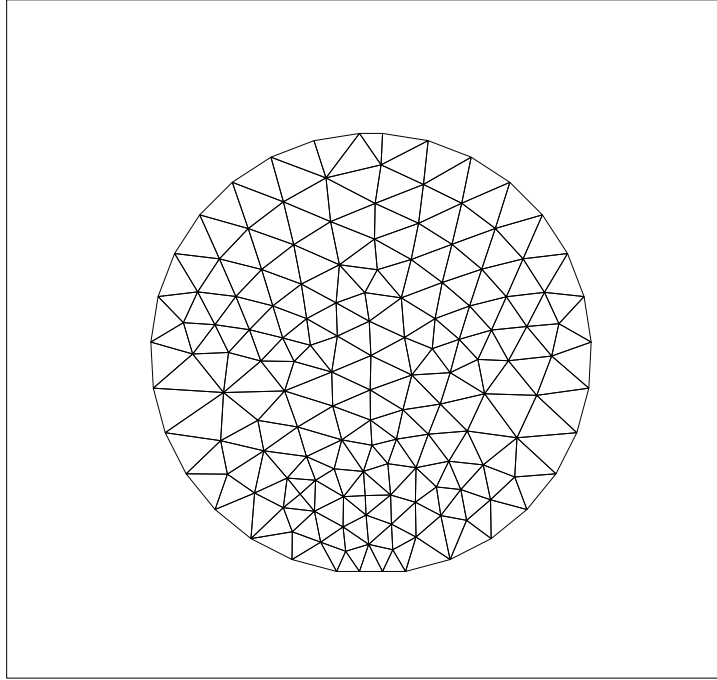


Figure 5: Jet circulation in a reservoir: computational mesh

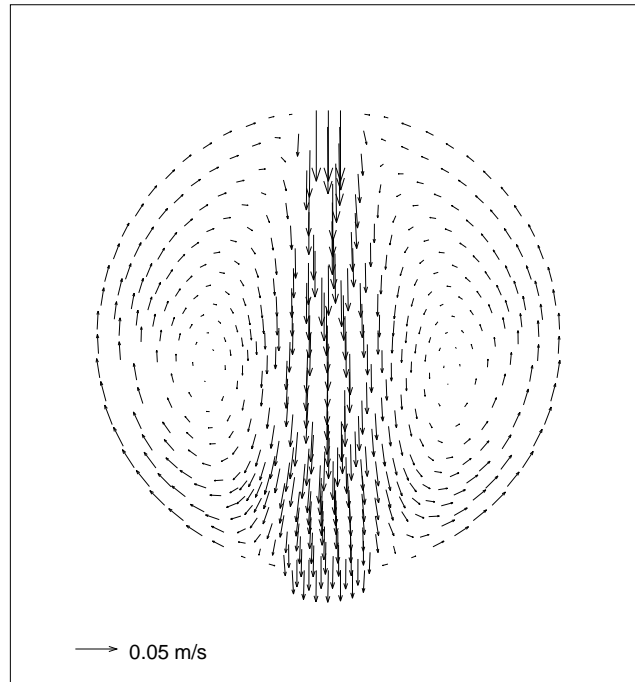


Figure 6: Jet circulation in a reservoir: velocity field



$$h_0(x) = H + \gamma x - \frac{Q^2}{2g} \left( \frac{1}{H^2} - \frac{1}{(H + \gamma x)^2} \right), \quad (87)$$

where  $H$  and  $\gamma$  are constant values, it can be easily verified that the equation (86) has the following exact solution:

$$h(x) = H + \gamma x, \quad q(x) = Q. \quad (88)$$

This test case allows for the verification of the accuracy of the scheme when a strong gradient is present in the bathymetry, as often occurs in rivers.

The computation for this test has been carried out using an inflow depth  $H = 4$ , an inflow unit-width discharge  $Q = 4$  and a bottom slope  $\gamma = 0.06$ . Although this test is essentially one-dimensional, an analogous case for the 2D code has been run on a channel 300 m. long and 4 m. wide. The computational mesh is almost regular, it is composed by 580 elements and a detail of it may be seen in Figure 7.

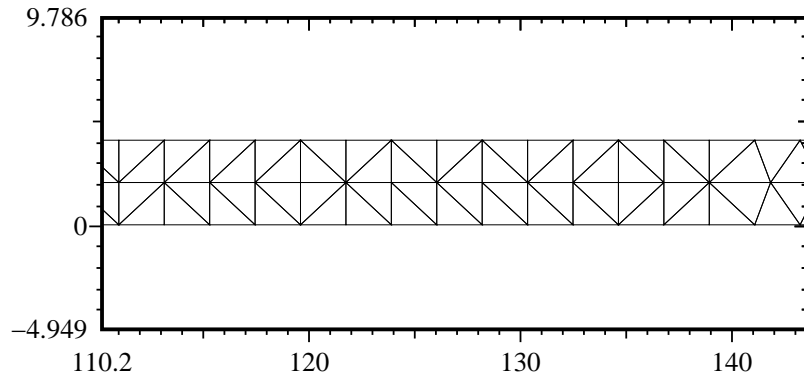


Figure 7: A detail of a regular mesh used in test case 2.

For the boundary conditions, the value of  $Q$  has been imposed at the inflow whilst the value of  $\xi$  has been imposed at the outflow. Figure 8 contains two graphs: a plot of the exact elevation versus the computed elevation and a plot of the computed unit-width discharge. The former plot evidences the good accuracy of the scheme for the elevation as well as the fulfillment of the mass conservation property with a small loss of 0.5% for this mesh.

It should be mentioned that a very large number of time steps were required to reach the steady state solution, since no mechanism to dissipate the spurious components of the initial conditions is present in this computation.



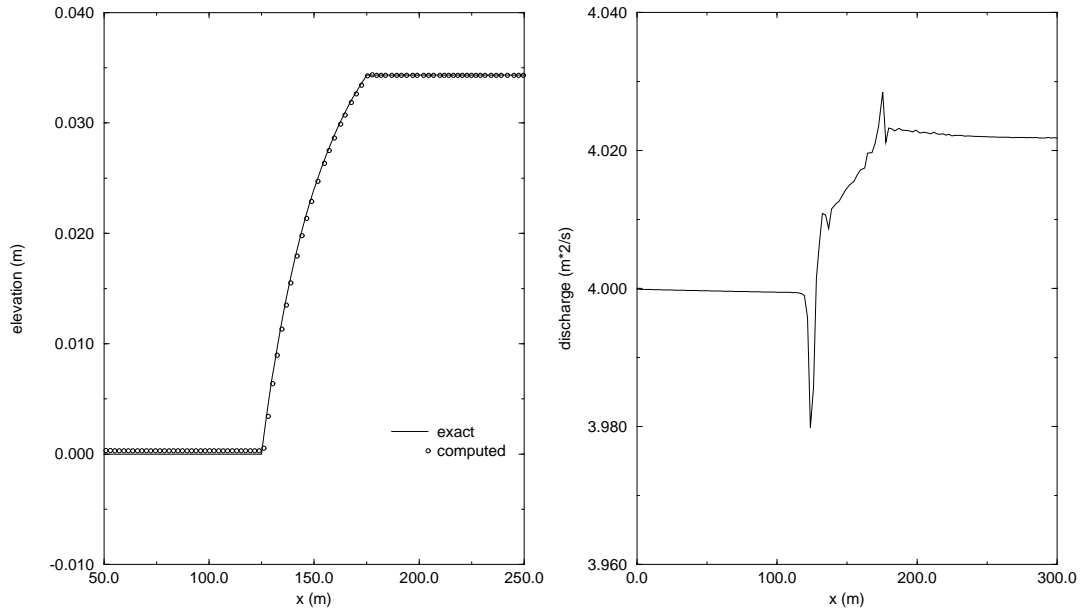


Figure 8: Water elevation and unit-width discharge for the 1D test case.

### 11.3 Parallel Computation on a Complex Geometry

The parallel code has been used for the simulation of the marine circulation in the *Bocche di Bonifacio*, the strait separating the Corsica and Sardinia islands in the Mediterranean sea. In this model, it is assumed that no stratification occurs and that the water circulation is essentially driven by the tidal boundary conditions, the wind stress and the Coriolis force. This hydrodynamic problem is characterized by a substantial complexity of the geometrical data.

We have used a mesh composed of 75053 elements and 38303 vertices. The total unknowns of the problem are 38303 elevation nodal values and 151661 discharge nodal values (for every component). The size of this problem does not fit into the memory of a single processor (with 128 MB of RAM), and a minimum of two processors of an IBM-SP2 must be used.

We first analyze the numerical behavior of the Schwarz algorithm with respect to the number of sub-domains. In Figure 10 is shown the CPU time required by one global CG iteration versus the number of sub-domains  $N_s$ , for a fixed number of processors. The Schwarz algorithm runs faster when a large number of sub-domains is used, until the communication overhead for the global CG becomes relevant, eventually preventing further time savings.

To evaluate the overall code performance, this result has to be considered together with the result shown in Figure 11, where we illustrate how the number of global CG iterations varies with the number of sub-domains. The preconditioning capability of the



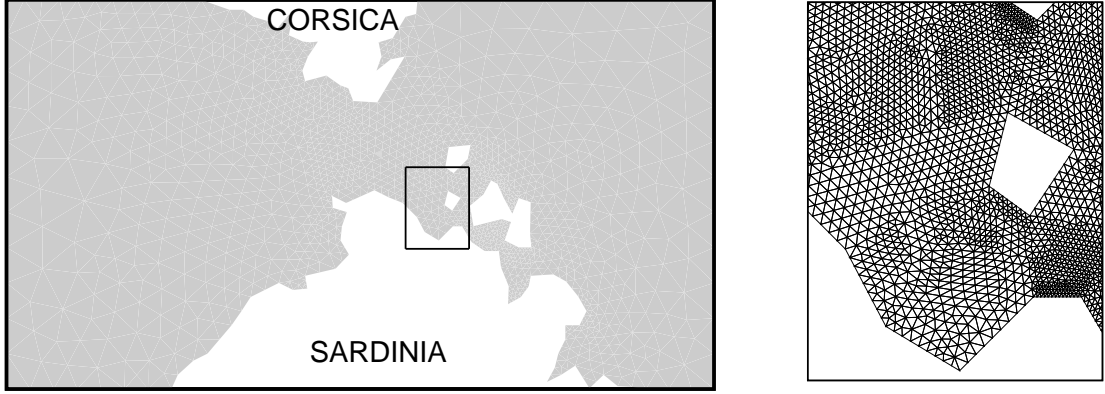
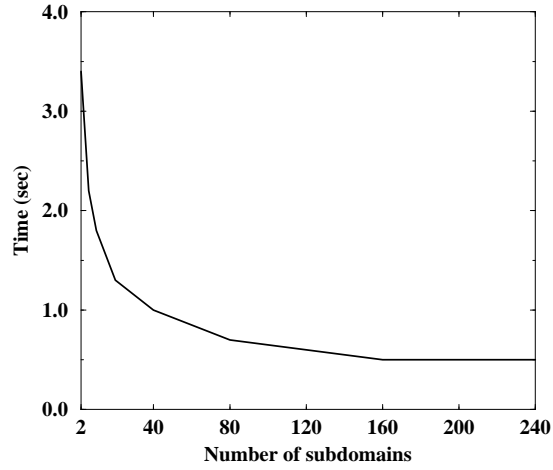


Figure 9: On the left: the computational domain for the Bocche di Bonifacio test case. On the right: a detail of the computational mesh for the zone indicated in the left figure. The entire mesh has 75053 elements.





original Schwarz algorithm degrades when the number of sub-domains increases. However, the algebraic coarse grid correction halts this degeneration completely when more than ten sub-domains are used. By joining the results shown in Figures 10 and 11 we obtain the curve for the total CPU time needed to solve the linear system, versus the number of sub-domains, for a fixed number of processors (Figure 12). The best performance for the present test case has been obtained with 200 sub-domains. This result demonstrates the usefulness of choosing the number of sub-domains independently from the number of processors actually used in the calculation.

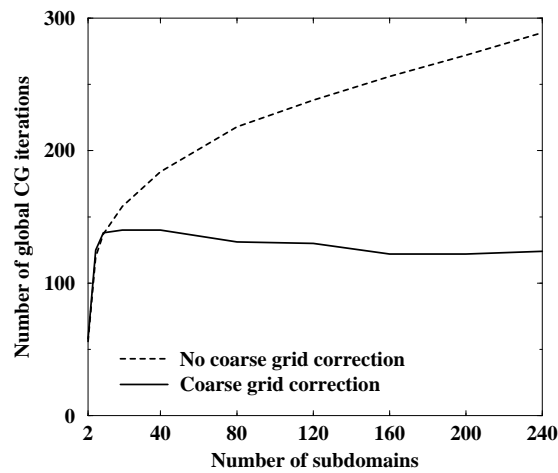


Figure 11: Schwarz preconditioning: number of global CG iterations required to reach convergence versus the number of sub-domains  $N_s$ .

We now examine the parallel performance of the code, by varying the number of processors and keeping fixed the number of sub-domains for the Schwarz preconditioner; in the present case, we have used the partition of 200 sub-domains.

In Figure 13 the total speed-up of the shallow water code is shown. As it can be noticed, both the Lagrangian integration and the Step 2 integration (which are explicit) show a speed-up which is very near to the ideal one. The speed-up of the implicit step, while not being ideal, is however satisfying. Since this step has the major computational cost, its behavior reflects largely on the total speed-up (continuous line). The odd behavior of the curve (the first derivative does not decrease monotonically, as it would be expected), is due to the particular setup of sub-domains we use: the shape of the sub-domains for the preconditioning step changes every time the number of processors changes, even if their number and size do not. Thus, since the speed and the preconditioning properties of the Schwarz algorithm can be influenced also by the shape of the sub-domains, we can need different numbers of iterations for the global CG to reach the given convergence threshold.

In order to further test the behavior of the Schwarz algorithm, we have run the same



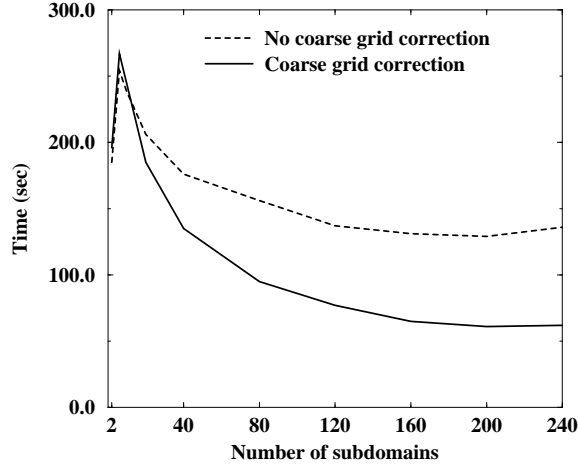


Figure 12: Schwarz preconditioning: CPU time required to achieve convergence of the conjugate gradient solver versus number of sub-domains  $N_s$ , using two processors.

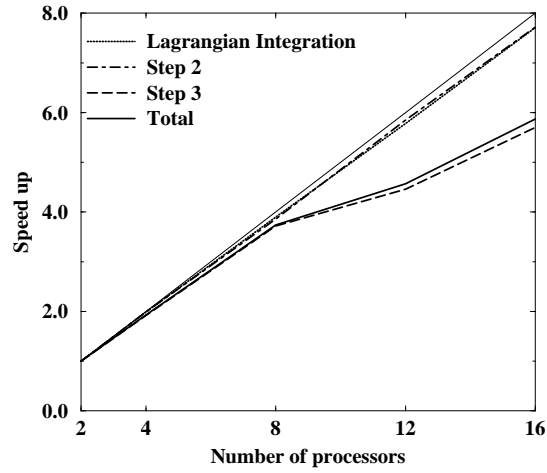


Figure 13: Speed-up of the whole shallow water code, for the mesh composed by 75053 elements. Due to memory requirements, this problem runs on a minimum of two processors, so the speed-up are normalized by the two processors value; the ideal speed-up for 16 processors is thus 8.



problem on a coarser mesh, to have the possibility of also performing the simulation on a single processor. The sequential code has been run using an efficient preconditioner, that is an Incomplete LU decomposition (ILUT). The reduced mesh is composed by 39170 elements and 20169 vertices. We have done both serial and parallel runs, using a RISC processor of the system IBM-SP2, with 128 MB of RAM. In Figure 14 we report the timing

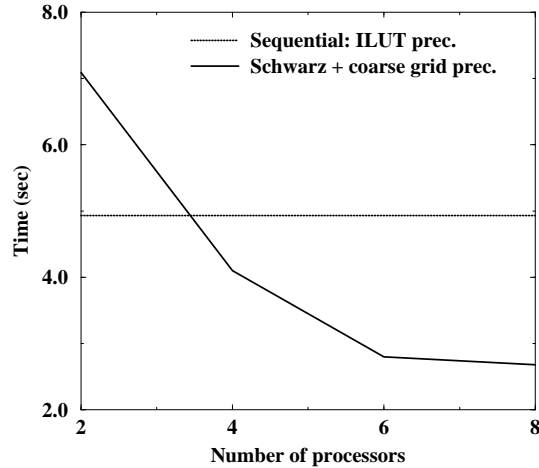


Figure 14: Implicit step: time for the solution of the linear system, on a mesh of 39170 elements. The horizontal line refers to a sequential run, using an ILUT preconditioner. The other curve refers to parallel runs, on 2, 4, 6 and 8 processors, with the Schwarz preconditioner.

for the solution of the linear system at the implicit step. The horizontal line represents the time needed by the scalar run, for the case with ILUT preconditioning. We can see that the Schwarz preconditioning gives better performance with respect to the sequential ILUT algorithm when more than three processors are used.

#### 11.4 Abrupt enlargement of a channel; the $k - \epsilon$ model

To validate the  $k - \epsilon$  model described above, it has been chosen the test case discussed in [35], corresponding to the flow in an abrupt enlargement of a prismatic channel. The geometry of the problem may be seen in fig.1; it has been supposed that the channel is 4 meters deep and the incoming flow has unit width discharge of 3 square meters per second. The flow is expected to separate at the edge of the enlargement, with consequent recirculation.

The most interesting aspect to be compared with experiments is the length of the recirculation zone: the reattachment length for a geometry as the one showed in in fig.15 should be slightly less than six times the width of the enlargement, if the ratio of the width of the former part of the channel over the depth is nearly one [36]. It is worthwhile



to remark that such an estimate assumes no dependence of the reattachment length on the roughness of the channel and on the inflowing velocity.

The velocity field plotted in fig.17 shows that the computed solution has a reattachment length which is smaller than the expected one. This is accordance with the results showed in [35].

The use of wall functions, at least when using a mesh not stretched at the boundary, yields to a negligible production of turbulent quantities at the wall. The turbulent kinetic energy is essentially produced at the enlargement of the channel, because of the transversal stresses in the fluid. In such region is the maximum of turbulent kinetic energy, which is about 0.03 square meters per square second. The poor performance showed by the  $k - \varepsilon$  model is in accordance with the well known inability of the method to simulate separated flows.

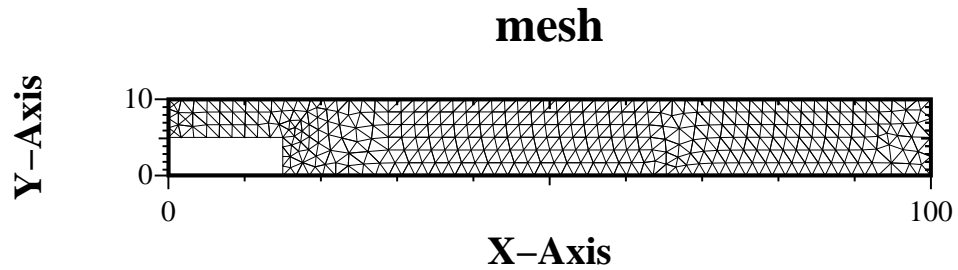


Figure 15: Prismatic channel with an abrupt enlargement: computational mesh.

### 11.5 Automatic Mesh Adaption: steady state case

To investigate numerically the performance of the mesh adaption strategy outlined above, it has been chosen a test case involving several characteristic features of shallow water flow.

In fig.21 may be seen the geometry of the channel and the initial computational mesh used for the present calculations. The test is designed to collect in a sketchy fashion a number



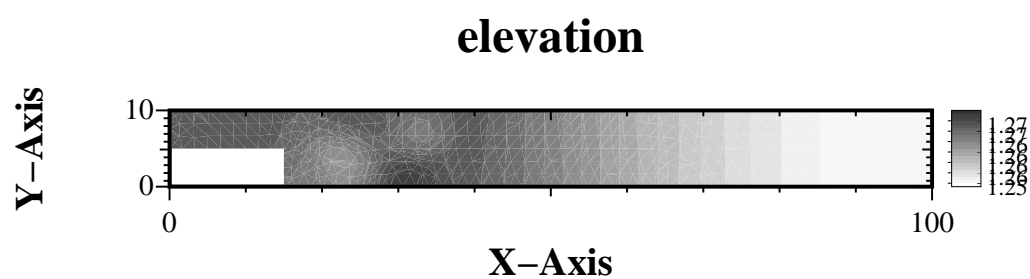


Figure 16: Prismatic channel with an abrupt enlargement: water elevation.

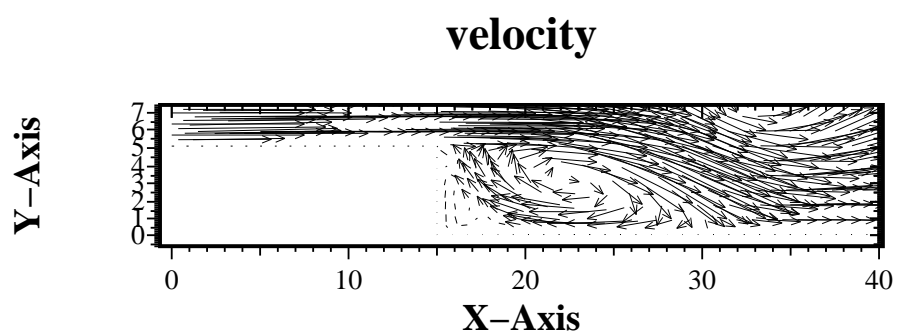


Figure 17: Prismatic channel with an abrupt enlargement: velocity field.



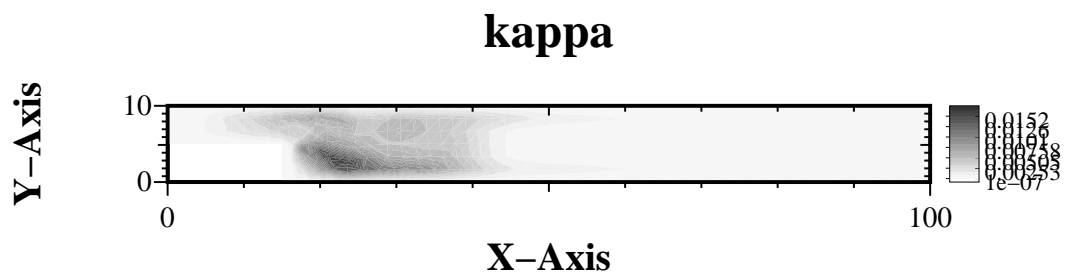


Figure 18: Prismatic channel with an abrupt enlargement: turbulent kinetic energy.

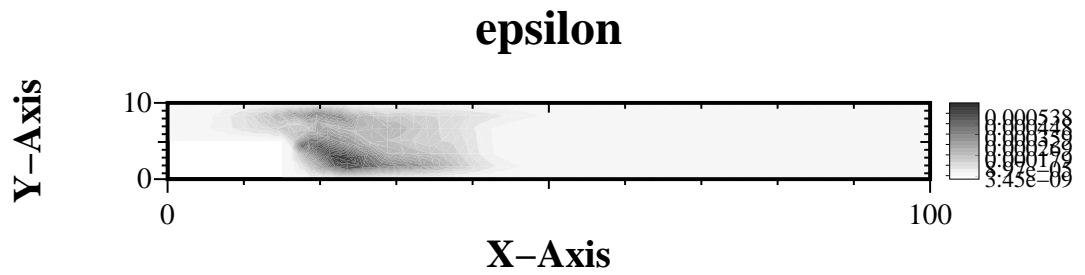


Figure 19: Prismatic channel with an abrupt enlargement: rate of dissipation of turbulent kinetic energy.



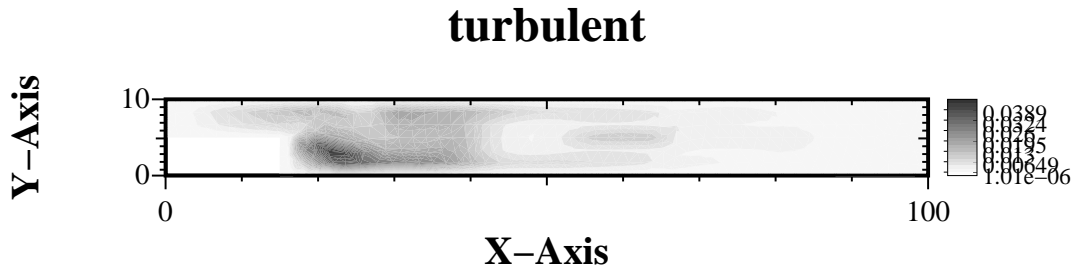


Figure 20: Prismatic channel with an abrupt enlargement: turbulent viscosity.

of typical situations that occur in river flow. The main channel is 2 kilometers long and 100 meters large, it has an abrupt enlargement that doubles its width, a smaller inflowing branch, a square island in the middle. In the initial part the bottom of the channel has a constant depth of 3 meters, in the final part the depth rapidly becomes 6 meters. The inflow boundary conditions of the main channel and of the secondary channel are 300 and 100 cubic meters per second, respectively. At the outflow a constant water elevation is imposed.

The initial computational mesh is intentionally quite coarse, being composed by 120 nodes only. In fig.22 it is shown the velocity field computed on the background grid. The simulation performed on the initial grid does not reveal recirculations neither behind the abrupt enlargement nor behind the island.

It has been chosen to refine the initial grid adaptively up to three levels of refinement, the final mesh being composed by about 370 nodes. In figg.23-25 are shown the refined meshes obtained by using different error indicators.

The use of the error indicator  $\epsilon_1$ , based on water elevation derivatives, leads to the mesh plotted in fig 23. It can be seen that the shear layer at the left corner of the inflow of the smaller channel is not devised by the error indicator as a zone to be refined. The channel enlargement, the right corner between channels and the bottom jump are slightly refined, but most of the new triangles are posed around the island, mainly behind.

When using the error indicator  $\epsilon_2$ , the secondary channel inflow, the bathymetry slope



and the region around the stagnation point are not detected as zones to be refined. The refinement is deserved for regions around detachment points, that is zones with larger velocity shear.

The error indicator  $\epsilon_3$ , based on local mass conservation, refines all the regions that the other error indicators detect one by one. The global mass error performed by the coarse initial mesh, defined as the difference between the inflowing and the outflowing water, was about 3%. By using the grid refined as driven by the  $\epsilon_4$  indicator, the mass defect is reduced to 1%.

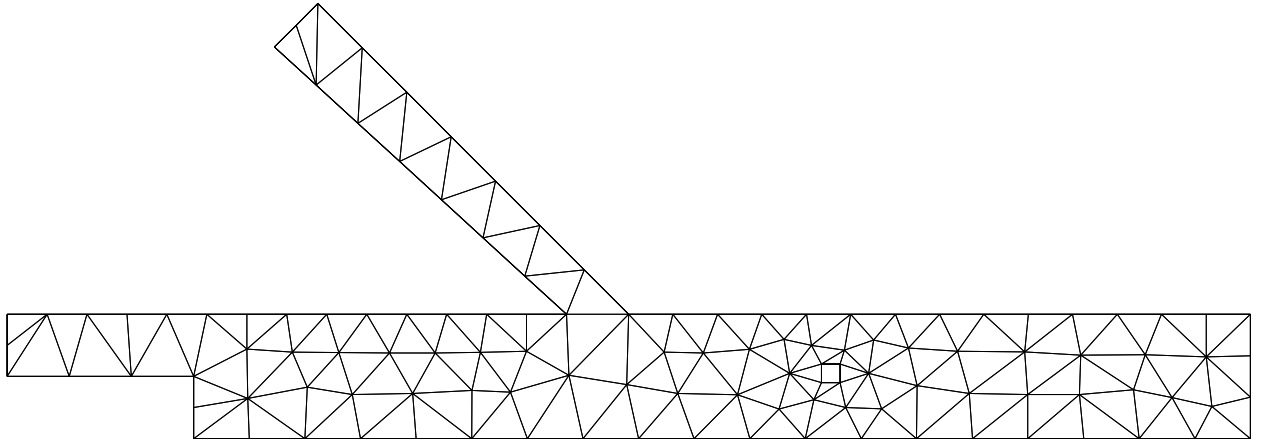


Figure 21: Background mesh.

To get a quantitative evaluation of the quality of the adaptively refined meshes, the shallow water code has been run on a grid obtained refining uniformly three times the background grid, up to a final number of elements which is 64 times the initial one. The numerical solution computed on the finest grid is then taken as the reference one: the truncation error is evaluated comparing the water elevation and velocity computed on the finest mesh and the values computed on the adaptively refined meshes. The figs.26-27 show plots of the error, defined as

$$\hat{\eta}_\xi = \frac{(\bar{\xi} - \xi)}{\bar{\xi}}, \quad \hat{\eta}_v = \bar{v} - v, \quad (89)$$

where  $\bar{\xi}$ ,  $\bar{v}$  is the reference solution computed on the finest grid. The absolute value of the velocity error is considered, not to overestimate the contribution due to the stagnation



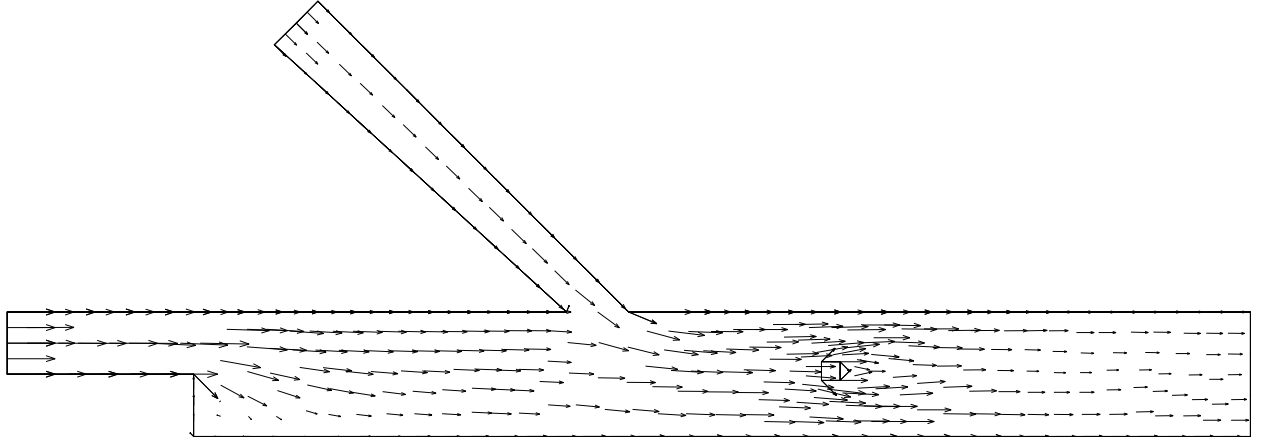


Figure 22: Velocity field computed on the background mesh.

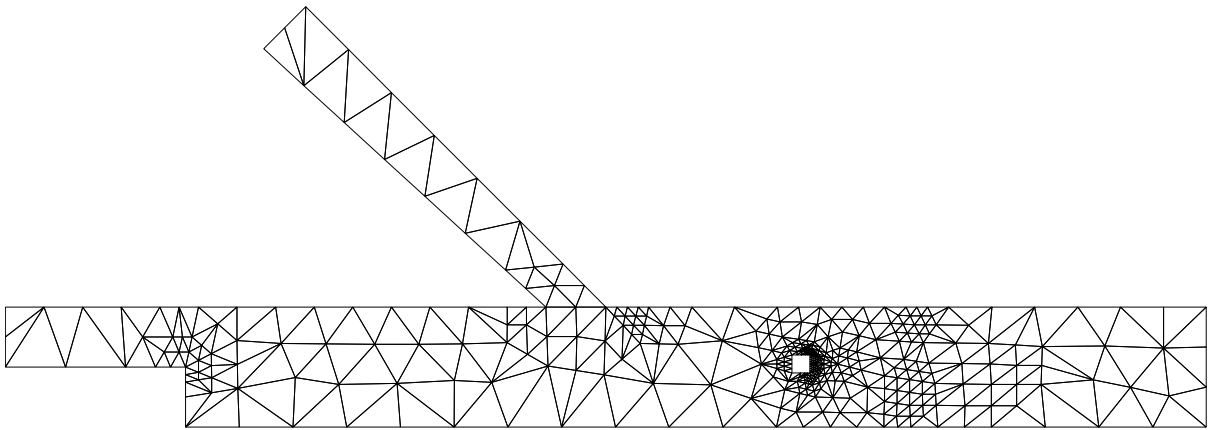


Figure 23: Refined mesh obtained using the error indicator  $\epsilon_1$ .



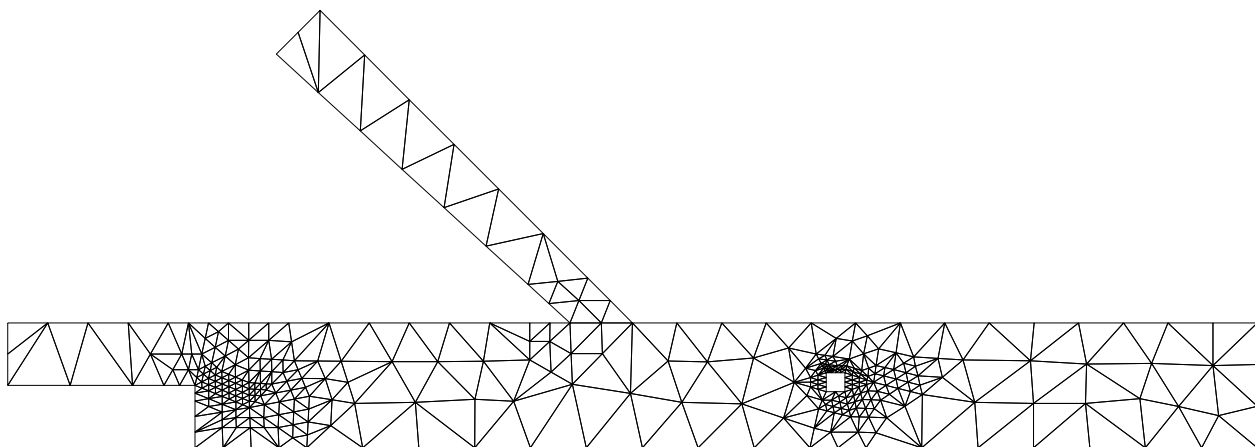


Figure 24: Refined mesh obtained using the error indicator  $\epsilon_2$ .

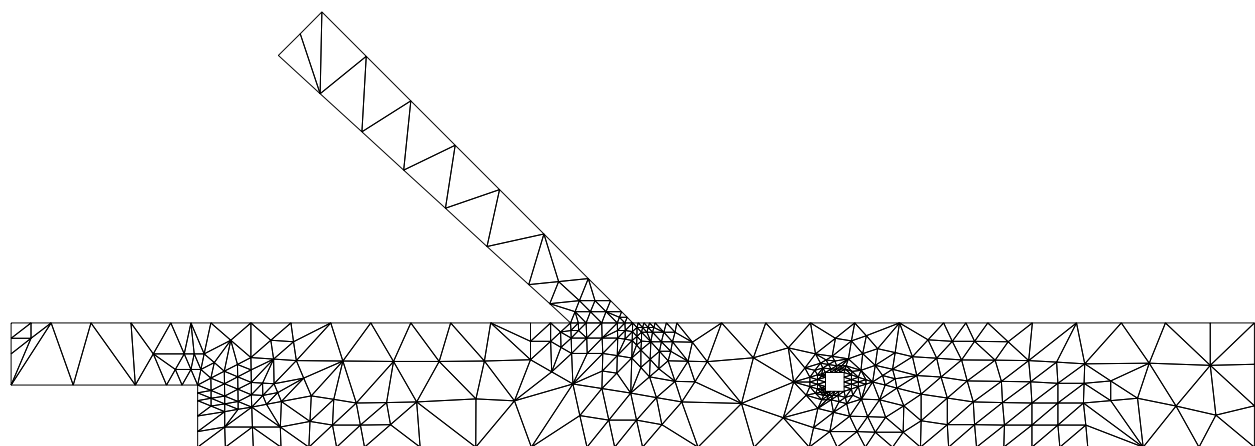


Figure 25: Refined mesh obtained using the error indicator  $\epsilon_3$ .



points.

Generally speaking, in all the simulations the bigger error is located around the island, that is the region mostly refined in all the the adapted meshes. Moreover, the results plotted in figs.26-27 show that both globally and locally the error indicator  $\epsilon_3$  performs better in computing the water elevation and gives better global results in computing the velocity field.

error indicator	$\xi$ (%)	$v$ (m/s)	$v$ direction (rad)
none	6.1	0.17	0.22
$\epsilon_1$	3.1	0.06	0.08
$\epsilon_2$	2.6	0.08	0.18
$\epsilon_3$	0.5	0.03	0.03

Table 1: Average error of the computed solution.

The maximum relative error in the water elevation is 5 % and is located behind the island; this value is lower than 8 % and 10 % obtained by the other criteria. In particular, the error indicator  $\epsilon_1$  show large errors both at the corner of the enlargement and at the left inflow corner. The error indicator  $\epsilon_2$  show a large error at the left inflow corner. The global behavior of  $\epsilon_3$  is even better, showing in most of the domain an error of 0.5 %, versus 2-5 % given by the other criteria.

The error in the magnitude of the velocity suggest more or less the same remarks. The maximum error induced by the criteria  $\epsilon_1$  is slightly larger than the others, but it is strongly confined around the island. The other indicators lead to a relevant error also near to the right inflow corner of the secondary channel.

The numerical tests show that mesh adaption is a very reliable tool for numerical simulation of shallow water steady flows. Any error indicator yield to numerical results that are strongly improved with respect to a uniform mesh, with a minor increase in the computational effort. The mesh refinement-coarsening technique is almost decoupled from the numerical integration aspects. Last, but not least, the initial mesh generation does not require any a priori knowledge of the flowfield, as any quite regular background grid is automatically refined to an almost optimal one.

Although the numerical results have been obtained for a test case that has been thought to include more scenarios, general conclusions can be hardly drawn. However, it is possible to say that all error indicators do their own job, detecting regions where truncation error is relevant. The local mass conservation criteria performs better in the considered test case, yielding always to lower error in a global sense. The reason of this behavior is probably



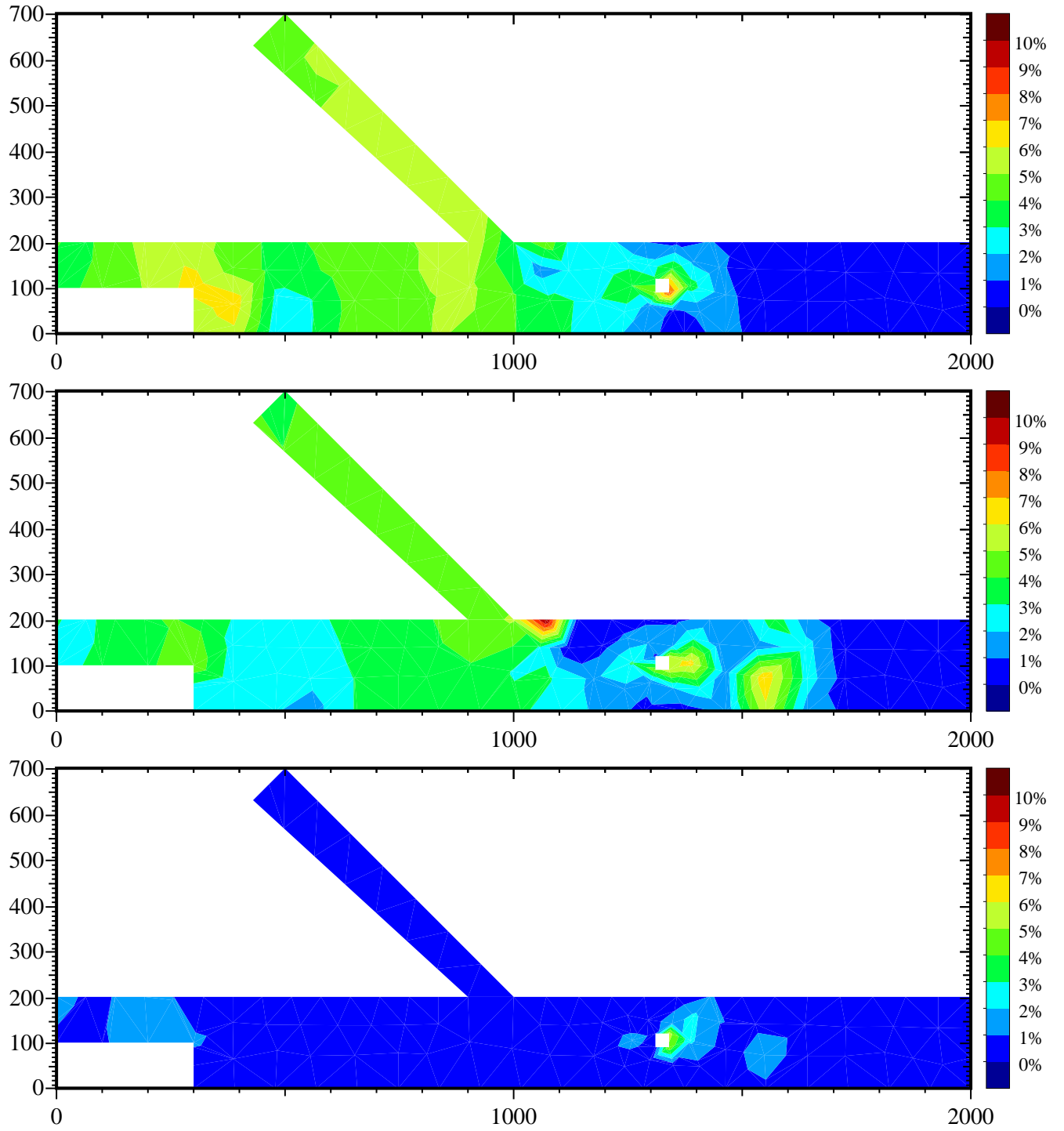


Figure 26: Relative error in the water elevation value obtained by using the refined grids of figures 23-25.



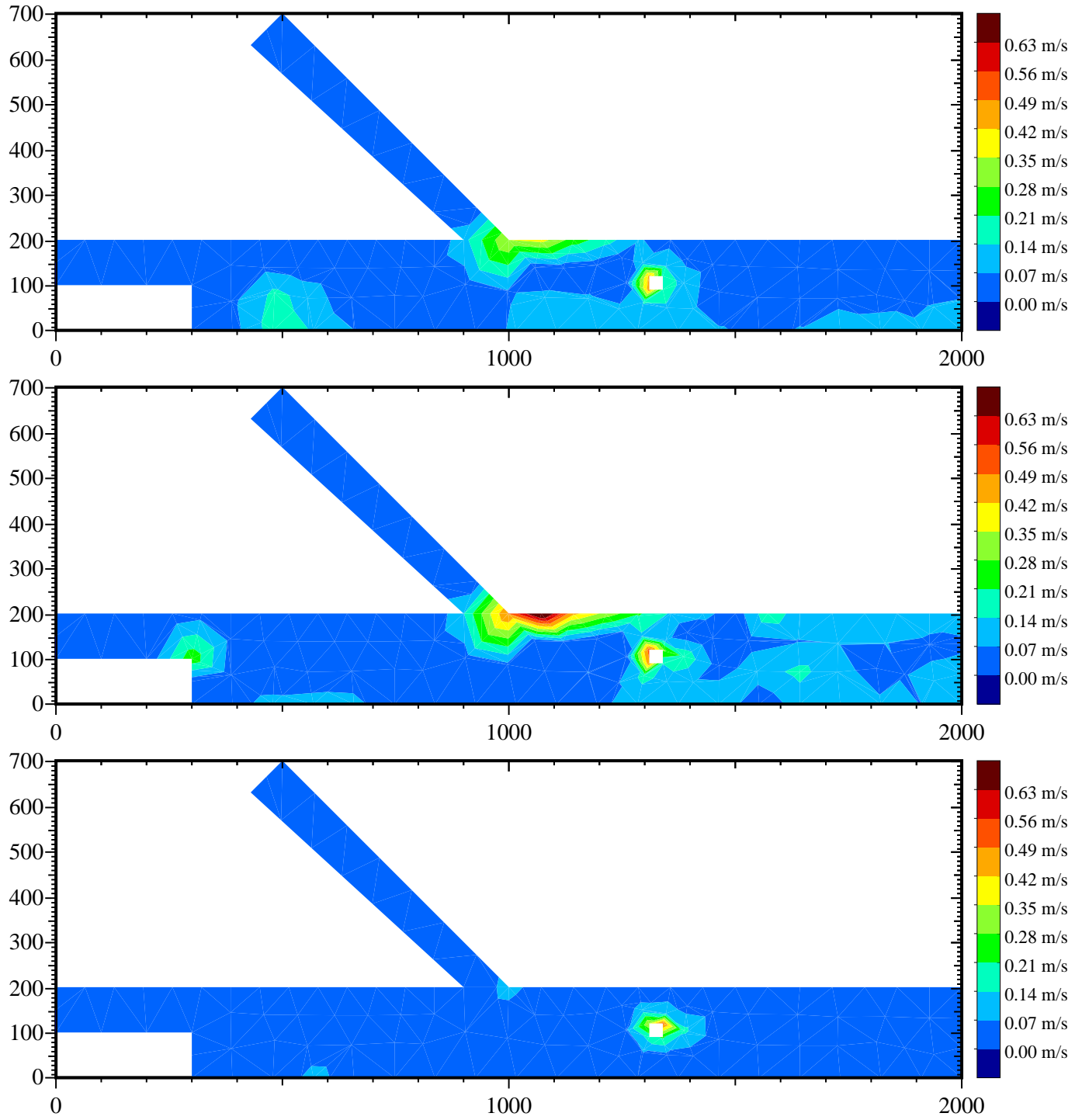


Figure 27: Absolute error in the magnitude of the water velocity obtained by using the refined grids of figures 23-25.



that only mass defect check involves both the unknowns (velocity and elevation) of the problem.

## 11.6 Automatic Mesh Adaption: unsteady state case

To further investigate the performance of the error indicators and of the adaption procedure in the case of unsteady flow, we chose a case of circulation in a closed basin induced by a tidal current. This kind of problem, commonly studied using SWEs, have a great environmental interest. An example is the coupling of a SW code with a transport model of nutrients, as nitrogen and phosphorus, enable to recognize conditions leading to eutrophication and then to anoxic crisis, in basins characterized by a long time of retention [33].

The domain used is the same of the steady state case (see Fig. 21); this time the two inflowing branches to the left are closed, and the elevation, measured in meters and imposed on the right open boundary, is given by the following expression:

$$\xi(t) = \frac{1}{2} \left[ \cos \frac{2\pi t}{24} + \cos \frac{2\pi t}{12} \right] \quad (90)$$

This BC simulates the ideal case of a tide of about one meter of amplitude, typical of the Mediterranean area, with a period of 48h due to the superimposition of a period of 12h and one of 24h (see Fig. 28).

Some general considerations can be made about the solutions of such a problem. First of all, the values of the elevation field will be very high almost all the time because they are imposed in all the domain by the amplitude of the tide ( $\sim m$ ). On the contrary the values of the velocity, and therefore of discharge, will be very small because the tidal current varies very slowly ( $\sim 12h$ ).

To have an idea of the amplitude of the true error of the numerical solution, we performed a run using the background mesh of Fig. 21 (*fine0* solution), and then another run using the grid obtained by uniformly refining three times the previous one (*fine3* solution). These grids are the same we described in the previous section.

Using *fine3* as reference solution, we calculated the maximum relative deviation between the two solutions as:

$$\epsilon_{rel}^{max} = \max_{x,y,t} \frac{abs(fine3(t) - fine0(t))}{\max_{x,y} abs(fine3(t))} \quad (91)$$

where *fine* can be either  $\xi$  or  $q$ .

The more interesting result is that the maximum deviation for the elevation is very small ( $\simeq 10^{-4}$ ) but that of the module of the discharge is not negligible ( $\simeq 0.33$ ). The fact that the deviation of  $\xi$  is so small makes very difficult, if not useless, the location of



the elevation errors, in this particular case. The deviation of the module of the discharge is instead consistent, but -as already- remarked absolute values of discharge in this test are very small. These observations should highlight the capability of the chosen test case to assess the goodness of the error estimators and of the whole adaption procedure.

If with the refinement of the background mesh the numerical solution is converging toward the exact one, and *fine3* can be considered a good estimate of the exact solution, then  $\epsilon_{rel}^{max}$  can be thought as an estimate of the maximum relative error of the *fine0* solution. A qualitative proof of the convergence of the numerical solution has been obtained comparing the solutions *fine0* and *fine3* and those obtained refining the background mesh uniformly one and two times (*fine1* and *fine2* solutions). The maximum deviation for the module of the discharge of the solutions *fine1* and *fine2* are respectively  $\simeq 0.12$  and  $\simeq 0.06$ . This seems indicate with good certainty that with the progressive uniform refinement of the mesh the solution is converging and that *fine3* represents a quite accurate solution. For this reason from now on with the sentence "estimated true error" we will refer to the difference between a generic and the *fine3* solution, evaluated on the nodes of the background mesh.

To verify the performance of the three error estimators proposed we have calculated the spatial correlation between these and the corresponding "estimated true error" for the solution *fine0*. The correlation is practically zero for the elevation due to the fact that the errors of the solution for this variable are negligible (see Fig. 28). The temporal evolution of the correlation for the module of the discharge, appears to be more interesting: this value generally being equal to about 0.8, but periodically falling to very low values. In the same figure we show the temporal evolution of the imposed elevation: periods of low correlation are in correspondence with periods of stagnation of the tide ( $d\xi/dt = 0$ ). Near to these instants, velocity of the water, already very small is practically zero. For this reason, the fact of having obtained a low correlation should not be surprising, nor of concern: when the correlation is low all the estimated errors has a minimum (see also Figs. 29,30). Spatial correlation for the other two estimators (not shown) give similar results and for this reason we will use in the following tests only the estimator  $\epsilon_3$ . The criteria adopted during the adaption procedure is that described in section 10.2.1 with a call every 13 minutes. In addition we added the constraint of a maximum number of P1 nodes about 360. Temporal evolution of the mean value of the "estimated true error" of the module of the discharge is showed in figure 28. In the same figure we also show the errors of the solutions *fine0*, *fine1* and *fine2*.

The average errors for the *adapt* case are very near to those of the solution *fine1* (see also Table 2). Moreover, after about the first six hours of integration, during which there is a slow relaxation of the initial condition to the imposed boundary conditions, errors of the *adapt* solutions are between those of the solution *fine1* and the solution *fine2*. In Table 2 the errors, averaged spatially and temporally excluding the first six hours of integration, are shown. As can be seen, although mean number of nodes used in the *adapt* run is lower than that of the *fine1* run and about one fifth of that in the *fine2* run, the global errors



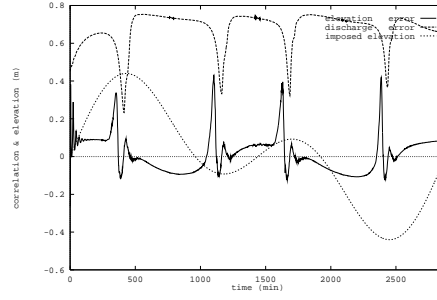


Figure 28: Spatial correlation between the  $\epsilon_3$  error estimators and the “estimated true error” as a function of the integration time. Dotted line is the imposed elevation expressed in meters.

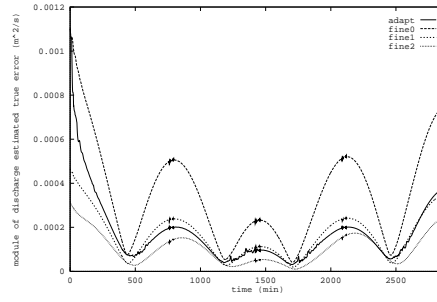


Figure 29: Average “estimated true error” of the discharge module as a function of the integration time; solutions *fine0*, *fine1*, *fine2*, *adapt*.

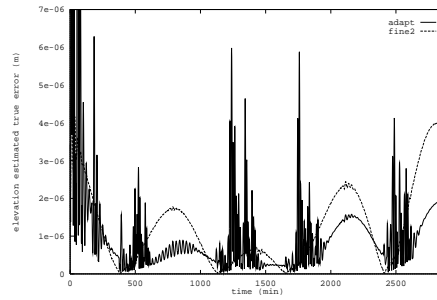


Figure 30: Average “estimated true error” of the elevation as a function of the integration time; solutions *fine2* and *adapt*.



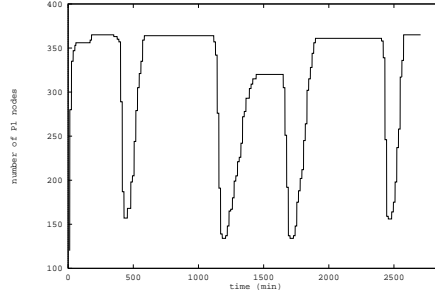


Figure 31: Number of P1 nodes as a function of integration time in the *adapt* case.

run name	$\overline{\epsilon}_{\xi} \cdot (10^{-4}m)$	$\overline{\epsilon}_q \cdot (10^{-2}m^2/s)$	$\overline{\epsilon}_v \cdot (10^{-3}m/s)$	NV
<i>fine0</i>	2.2	3.1	9.7	120
<i>fine1</i>	1.2	1.5	4.6	403
<i>fine2</i>	1.2	0.9	2.7	1458
<i>adapt</i>	0.9	1.3	4.6	310

Table 2: Average maximum and average “estimated true error” of elevation  $\xi$ , module of discharge  $q$  and of velocity  $v$ . NV is the number of P1 nodes in each of the meshes used; in the adaption case NV is the average number during all the integration. Only solutions after the first six hours are used in the temporal averages.

of the *adapt* solutions are between those of the other two. Another indication that the adaption procedure is working correctly can be deduced from Fig.31: the number of P1 nodes as a function of the integration time is proportional to the error (see also Figs. 29, 30).

The estimated true error of the elevation has instead a more complicated course; every time the mesh is changed and the interpolation procedure is executed, a high frequency component of unphysical noise is introduced in the solution. This has been also verified performing a run during which, at fixed time intervals of 13 minutes, we interpolate the discharge over P2 nodes without changing the mesh. Once more, in the case of tidal currents, this is not of concern, because relative errors of the elevation are very small; to verify whether this could be a real problem for the adaption procedure, an unsteady test case, in which the mean value of the elevation is smaller, should be conceived. Therefore, although the mean global error of the *adapt* solution is also smaller than that of *fine2* (Tab. 2), we cannot say in general that the elevation field of the first solution is more accurate than the one of the second solution.



## Part III

# User Manual

## 12 Structure of the Code

SWEET is partly written in Fortran 90. The use of the new Fortran standard allows to exploit some relevant features at the programming level. However, in order to maintain as much as possible the structure of the code, only the dynamic memory allocation is currently used in SWEET.

SWEET is composed by a `main` routine plus nearly sixty subroutines; some of them are optional or mutually exclusive, their execution depending from the flag set in the `datin` file. The role of each subroutine is described in the following list:

### Subroutines of SWEET

Initialization	
DATAREAD	reads the <code>datin</code> input file
MESHREAD	reads the <code>mesh</code> input file
REREAD	reads the restart file
READBATI	reads the <code>bati</code> input file for bathymetry (if <code>bati=1</code> )
NORMBOUND	computes the versors normal to the open boundary
INISPYSTORY	initializes the output files for time dependent problems
INITVAR	initializes the unknowns
INITFE	initializes the finite element machinery
INIGLOSTIFF	initializes the stiffness matrix
LISTBOUNDNODE	builds the list of the nodes that belong to regions of the open boundary characterized by different values of the index <code>inod</code>
LISTNEAREL	builds the topological lists useful to recover the pathline when performing the lagrangian integration
SPERELEVBOUND	reads the input Fourier amplitudes and frequencies of the elevation at the open boundary
ELEVBOUND	computes the elevation to be imposed as boundary condition
Step 1	
LAGRAN	computes the momentum transport by the lagrangian method
EVALUATE	evaluates the value of the velocity in a given point of the element



Turbulence Model	
KEPS_IMPL	the $k - \varepsilon$ turbulence model module
KEPS_WALL	boundary wall function for the $k - \varepsilon$
KLOCSTIF	local stiffness matrix for the $k$
K_RHS	rhs for $k$
KEPS_DIRBOUND	boundary condition for $k$ and $\varepsilon$
EPSLOCSTIF	local stiffness matrix for $\varepsilon$
EPS_RHS	r.h.s. for $\varepsilon$
Step 2	
STEP2	the Step 2 of the fractional step procedure in the case of consistent mass matrix (see eq. (50))
Q1LOCSTIFF	computes the local stiffness matrix for discharge at Step 2
QKNOWN	computes the right-hand side in the equation for discharge at Step 2
Step 2 (lumping)	
STEP2L	the Step 2 of the fractional step procedure in the case of lumped mass matrix (see eq. (50))
QKNOWNL	computes the right-hand side in the equation for discharge at Step 2 in the case of lumped mass matrix
Step 3 elevation	
STEP3XI	the Step 3 of the fractional step procedure for the elevation unknown (see eq. (53))
XILOCSTIFF	computes the local stiffness matrix for elevation at Step 3
XIKNOWNTerm	computes the right-hand side term in the equation for elevation
XIDIRBOUND	inserts the Dirichlet boundary conditions for elevation in the linear system
Step3 discharge	
STEP3Q	the Step 3 of the fractional step procedure for the unit-width discharge unknown when mass consistency is adopted (see eq. (51))
Q2LOCSTIFF	computes the local stiffness matrix for discharge at Step 3
ELEVGRAD	computes the right-hand side in the equation for discharge at Step 3
WALLNOSLIP	introduces the no-slip boundary conditions at the wall in the linear system
WALLSLIP	introduces the free-slip boundary conditions at the wall in the linear system
QDIRB	inserts the Dirichlet boundary conditions for discharge in the linear system



Step3 (lumping) STEP3QL	the Step 3 of the fractional step procedure the unit-width discharge unknown when mass lumping is adopted (see eq. (51))
Passive scalar SCALAR_IMPL SC_LOCSTIF SC_RHS SC_DIRBOUND	the passive scalar model local stiffness matrix for the tracer rhs for the tracer boundary conditions for the tracer
Common routines CGPREC BICGPRES GLOSTIFF	conjugate gradient iterative solver with diagonal preconditioning biconjugate gradient iterative solver with diagonal preconditioning inserts the local contributions into the global matrix
Output SPYSTORY BOUNDISCH REWRITE	writes the value of the unknown in the spy nodes (if <b>steady=0</b> ) computes the discharge through the open boundaries writes the restart file
Mesh Adaption INIVARS  BUILDSTRUCTURES ERRESTIMATE  ADAPTION MARKGRID  STOREOLDXYAND- FIELDS ADAPT  REFINE DEREFINE UREFINE	some variables used in the adaption module are initialized. It must be called once before any other call build all data structures (see section 14) one of the error indicators is used to estimate the error of the numerical solution is the main module that calls all the others an integer <b>ErrorFlag</b> , based on the error estimate is assigned to each triangle of the mesh all fields and nodes coordinates are stored to be used to interpolate fields on the new mesh de-refinement of triangles where <b>ErrorFlag</b> < 0, refinement of triangles where <b>ErrorFlag</b> > 0 refinement of triangles where <b>ErrorFlag</b> ≠ 0 de-refinement of triangles where <b>ErrorFlag</b> ≠ 0 all the triangles of the mesh are standard refined



INTERPOLATE- FIELDSON- P2NODES	All physical fields in the new P1 nodes are obtained using values on the old P2 nodes. If a new P1 node was not an old P2 node then the value is obtained with the proper interpolation.
ADDALLP2NODES	all P2 nodes are queued to vel
DEREFINEALL	the mesh is completely de-refined. The final mesh will be the background mesh
STANDARDREFINE	standard sub-division of an element
GREENREFINE	green subdivision of an element
GREENREREFINE	a green element is replaced with one standard refined
MAKEGREEN	a standard element is green-refined (midpoint of an edge is joined with the vertex opposite to it).
STANDARDEREFINE	central triangle of a standard refined element is deleted and replaced by the father
GREENDELETE	a green pair of triangles is replaced by the father
GREENDEREFINE	replacement of a standard refined element with the pair of green triangles which have generated it

In addition to the routines listed above, the parallel version of the code has several new routines. Mainly they are parallel versions of corresponding sequential routines: in this case their name is simply `pa_*` or `*_pa`, where `*` stands for the name of the sequential routine. The parallel code has also some new routines, related to the Schwarz preconditioner for the conjugate gradient at Step 3. These routines will not be explained in detail.

PA_MAKELIST	build the communication lists
COMM	ensemble of communication routines
PARINIT	initializes the parallel environment
MULT_TEST_RUN	access the parallel CG code (substituting PA_CGPREC)

## 12.1 Flow Chart

In Figure 32 it is shown a schematic flow-chart of SWEET, sketching the structure of the `main` program. The figure refers to the sequential code, being the flow-chart of the parallel code very similar.

## 13 List of the Vectors

The role of many vectors of the code SWEET is explained in the code. However, for sake of simplicity, we list here a short description of the principal vectors that are introduced in the `main` of the code. The names of the vectors follow the standard Fortran rule:



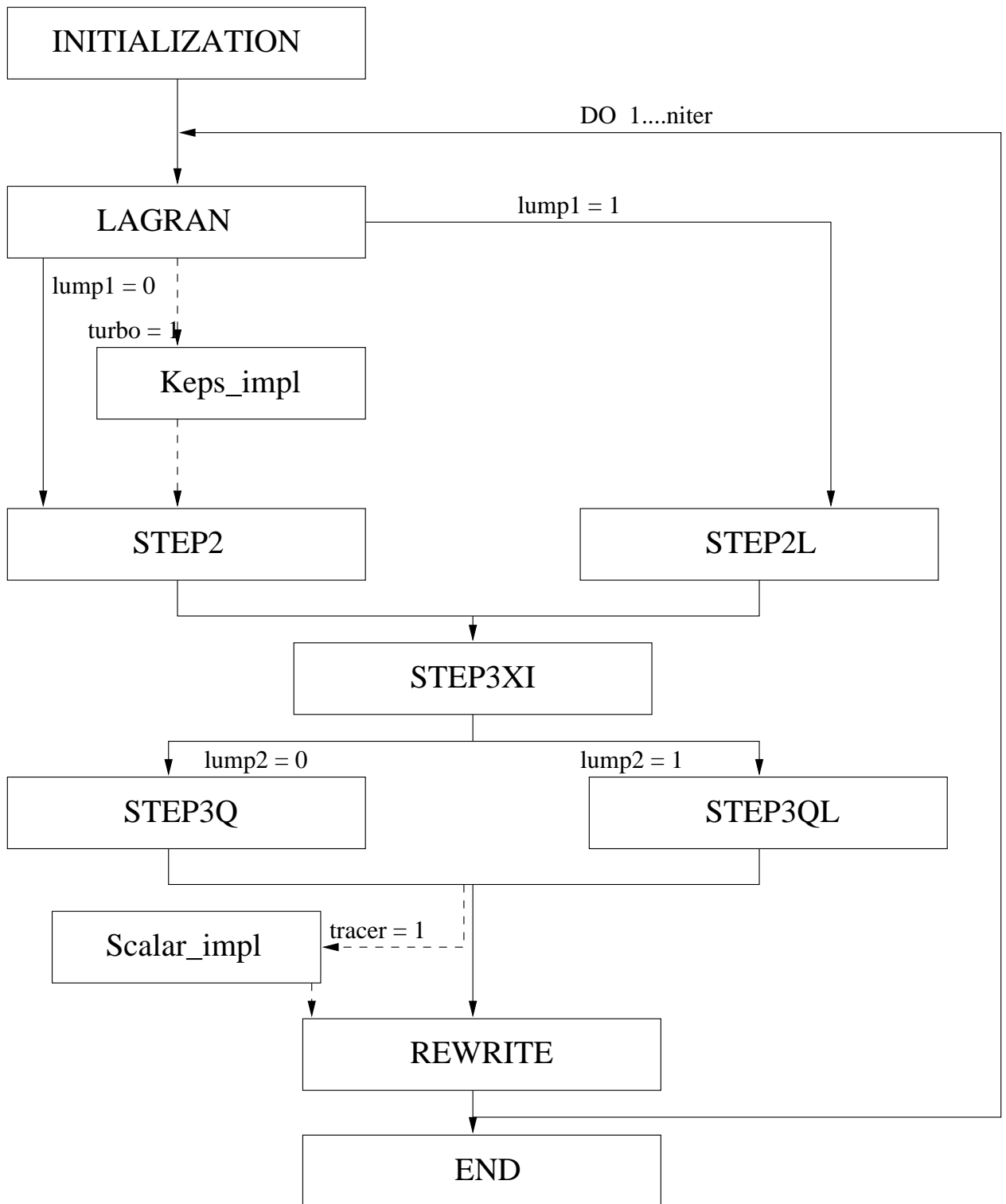


Figure 32: Flowchart of the code SWEET



the names beginning with *i,j,k,l,m,n* are *integer\*4*, the others are *real\*8*. All the physical quantities are measured in SI unit system.

<i>x(k,j)</i>	<i>k</i> -th coordinate of the node <i>j</i>
<i>slmax(j)</i>	maximum side length of the triangles surrounding the node <i>j</i>
<i>slmin(j)</i>	minimum side length of the triangles surrounding the node <i>j</i>
<i>h0(j)</i>	depth of the bottom in node <i>j</i>
<i>lne(k,j)</i>	list of the elements surrounding the node <i>j</i>
<i>nen(j)</i>	number of the triangles surrounding the node <i>j</i>
<i>lee(k,i)</i>	list of the elements surrounding the triangle <i>i</i>
<i>nel(i)</i>	number of the elements surrounding the triangle <i>i</i>
<i>area(i)</i>	area of the element <i>i</i>
<i>dphi1(k,j,i)</i>	derivative along the coordinate <i>j</i> of the k-th P1 basis function in the element <i>i</i>
<i>dphi2(k,j,l,i)</i>	derivative along the <i>j</i> -th coordinate of the k-th basis function of the element <i>i</i> evaluated in the quadrature node <i>l</i>
<i>reint(i,j)</i>	integral of the product of the <i>phi01(i)*phi02(j)</i> shape functions divided by the area
<i>phi01(i,j)</i>	P1 basis function <i>i</i> on the reference triangle evaluated in the quadrature node <i>j</i>
<i>amas1(j,k,i)</i>	P1 mass matrix contribution of the element <i>i</i> in column <i>j</i> and row <i>k</i>
<i>amas2(j,k,i)</i>	P2 mass matrix contribution of the element <i>i</i> in column <i>j</i> and row <i>k</i>
<i>aloc(j,k)</i>	local mass matrix
<i>vn(k,j)</i>	component <i>k</i> of the versors normal to the boundary node <i>j</i>
<i>alump(j)</i>	lumped mass matrix in node <i>j</i>
<i>h(j)</i>	total depth of the water in node <i>j</i>
<i>xi(j)</i>	elevation of the water in node <i>j</i>
<i>xiold(j)</i>	elevation of the water in node <i>j</i> at the previous time step
<i>xipo(j)</i>	elevation to be imposed on the <i>j</i> -th part of the boundary
<i>v(k,j)</i>	component <i>k</i> of the velocity in the node <i>j</i>
<i>qx(j),qy(j)</i>	components of the unit-width discharge in the node <i>j</i>



<code>qxold(j),qyold(j)</code>	components of the unit-width discharge in the node <code>j</code> at the previous time step
<code>qxhalf(j),qyhalf(j)</code>	components of the unit-width discharge in the node <code>j</code> at Step 2 of the previous time step
<code>he(i)</code>	average bottom depth in element <code>i</code>
<code>inod(j)</code>	type of boundary of the node <code>j</code> ; the convention is as follows: 0 internal node 10001 wall 10002 discharge imposed 2000x (x=3,4..) elevation imposed 3000x (x=3,4..) corners between wall and elevation imposed boundary: velocity is zero but elevation is assigned
<code>e(j)</code>	error estimate of the numerical solution in the <code>j</code> -th element
<code>estory(i)</code>	average of the error estimate at time step <code>i</code>

In the parallel version of the code, the two components of the discharge vectors are collected in a unique vector, called `qxy`. Nodes belonging to overlapping elements have negative `inod` values.

## 14 Data structures

When implementing algorithms of grid refinement and de-refinement, an important role in determining computational efficiency is played by the data structures used.

In particular, when implementing the algorithm described in Section 10.2 one has to use efficient structures to determine which elements are adjacent to a given one, which edges delimit it and which side has given vertices. This information can be obtained using complex structures such as lists, trees, tables etc. [34]. Here we chose to use structures (see Table at the end of this section) as simple as possible taking into proper account the computational efficiency.

In the discussion which follows a general survey, complete but deliberately simplified, of the whole adaption module is given.

Information about which nodes must be refined is contained in a vector of integers named `IERR(NEL)`. If `IERR(i)>0` element `i` will be refined in standard way, creating a new node at midpoint of each of the edges of the element in hand. Coordinates of these new nodes are queued to the vector `XV` and the number of nodes is incremented. As one or more of these nodes could be already created when refining an adjacent element it is very convenient to dispose of structures that contain elements adjacent to a given one and containing the edges delimiting it. To build these structures in an efficient way we start with an array that is used in SWEET too, to solve the Lagrangian part of time step here named `VVER(MAXAD,NV)`. This structure contains for every vertex of the mesh all the elements which have this vertex in common (`MAXAD` is the maximum number of elements



adjacent to a node).

Starting from **VVER** we built the array **VSID(2,NSID)** which contain for every side of the mesh indices of its ending points (**NSID** is the number of sides in the grid). To make an efficient search of an edge, given the indices of the ending points, sides in **VSID** are specified in such a way that  $\text{VSID}(1,i) < \text{VSID}(2,i)$ , and  $\text{VSID}(1,i), i=1, \text{NV}$  is ordered in increasing order. A simple hash table can be realized using a vector of pointers (**PVSID(NV)**) to **VSID**, that contains for every vertex the pointer to the first side to which this vertex belong. Search of a side  $s$  of given ending point  $v_1$  and  $v_2$  can be made ordering index  $v_1$  and  $v_2$  in such a way that  $v_1 < v_2$  and search of  $v_2$  is started from the position  $\text{VSID}(2, \text{PVSID}(v_1))$ . Disposing of **VSID** and **PVSID**, **SEL(3,NEL)** which contains for every triangle indices of its three sides, can be easily calculated. Lastly, **EEL(3,NEL)** which gives for every element indices of adjacent elements, is calculated.

With these structure at our disposal, the refinement procedure does not present great difficulties because as already mentioned new nodes are added to the queue of the array coordinates **XV** and indices of new triangles to the queue of the **VEL** array.

The procedure of de-refinement is a little more complicated because, generally, when vertices and triangles are eliminated, holes are created in the structures which describe the triangulation. To avoid such a problem we have adopted a de-refinement procedure that, every time it is executed, re-builds the mesh, starting from the background mesh, excluding those elements marked to be de-refined. In this way the same structures and procedures used for the refinement can be used also in the de-refinement part of the code.

In order to be able to re-build the mesh one has to know exactly its "history", that is for every element which does not belong to the background mesh one has to know of which element it is son, and eventually of which element it is the father. Data structures more suitable to store such information is tree. In our code this structure, called **HISTORY**, is a vector of integers where the beginning of every refinement step is labeled by a zero. Refinement operations are listed sequentially in **HISTORY** storing indices of the elements created. The end of the re-refinement step, that is eventually the beginning of another, is labeled by a zero. Since a given element can be divided either in a standard way (four elements) or in a green way (two elements), these last case is distinguished storing indices of the new elements with negative sign (**etype**). The major drawback of this procedure is that when re-building the mesh, different indices, in the old and new mesh, can be given to the same triangle.

To avoid this problem we conceived a procedure of identification of the elements that on the basis of an integer permits us to locate the position and the relatives with the other elements. In fact, since the background grid is never modified, all the **NELI** elements of the initial grid can be indexed in a unique way. At the end of the first step of refinement, since a single triangle can generate only four, two or zero new triangles, the mesh can have at maximum  $4 \cdot \text{NELI}$  elements. It is possible then to identify in a unique way every triangle created (first level triangles) dividing a triangle of the background grid (zero level triangles) assigning to it a number between  $\text{NELI}+1$  and  $5 \cdot \text{NELI}$ . Similar considerations



can be applied to triangles of the second level, obtained from a triangle of the first level. These triangles will be identified using an integer between  $5 \cdot \text{NELI} + 1$  e  $21 \cdot \text{NELI}$ , and so on for the other levels of refinement.

Every time a new P1 node is created, all the physical fields are interpolated in the new position and the type of the node is determined. When the refinement procedure ends, with the eventual creation of green elements, the P2 nodes are created and they are queued to P1 nodes. Every time a new node is created an efficient search of the coordinates of this node is made between the coordinates of the nodes of the old mesh. If the new node was already in the old mesh then the old values of the fields are used, otherwise the proper interpolation is executed (quadratic interpolation for velocity and linear for the other fields).

Follows a summary of the principal data-structures used in the adaption module.

VVER(MAXAD,j)	elements adjacent to vertex j
VSID(2,j)	ending points of side j $\text{VSID}(1,j) < \text{VSID}(2,j)$
PVSID(j)	pointer to the the first side on VSID which has vertex j as first extreme
SEL(3,j)	sides of the element j
EEL(3,j)	elements adjacent to the element j
HISTORY	tree where history of the grid is stored
E_ID(j)	identifier of the element j
ETYPE(j)	level of refinement of the element j. if $\text{ETYPE}(j) < 0$ the element is green.

## 15 Sequential Input and Output

In the SWEET package, it has been added an example application that is thought to be useful for starting up in using the code. In this Section we comment on which are the input and output files that are necessary to run SWEET and which is their format. We suggest to read this Section comparing to what is written in the given example and then running the example itself.

### 15.1 Input

The input files read by the code SWEET are

**datin** It is an ASCII file where are stored the informations concerning the different options that are to be run in the code. The content of this file is shown in the subsequent tabular. The format of the file can be deduced from the source of the code or from the enclosed example.



<code>dt</code>	time step
<code>niter</code>	number of time steps
<code>turbo</code>	if 1, $k - \varepsilon$ turbulent model is used. In this case, <code>lump1</code> is switched to 0 (implicit diffusion).
<code>visc0</code>	eddy viscosity. If <code>turbo=1</code> it is an initial value.
<code>Strickl</code>	Strickler coefficient
<code>tracer</code>	if 1, passive tracer model is activated
<code>viscT</code>	if <code>tracer=1</code> , passive tracer diffusion coefficient
<code>bati</code>	if 1, reads bathymetry from the <code>bati</code> file (1), else assumes the uniform <code>h0</code> value
<code>rest</code>	if 1, reads the initial conditions from the file <code>restart.tem</code> , else uses <code>xi0</code> , <code>qx0</code> and <code>qy0</code> initial conditions
<code>steady</code>	if 1, steady state calculation, else unsteady (files <code>elev.time</code> , <code>disch.time</code> , <code>spy.nodes</code> must then be provided)
<code>wx,wy</code>	wind velocity components
<code>Coriolis</code>	Coriolis parameter
<code>h0</code>	constant bottom depth (when <code>bati=0</code> )
<code>xi0</code>	constant elevation of the water (when <code>rest=0</code> )
<code>qx0,qy0</code>	initial value of the discharge (when <code>rest=0</code> )
<code>xiX</code>	elevation to be imposed at the X-th boundary (when <code>steady=1</code> )
<code>qX</code>	discharge to be imposed at the X-th boundary (when <code>steady=1</code> )
<code>rk</code>	number of steps to be used to determine the pathline in the lagrangian integration of momentum
<code>itmax</code>	maximum number of iterations that can be performed to solve the linear systems
<code>tol</code>	maximum value of residual to stop the linear solver
<code>precond</code>	ignored by the sequential code. For the parallel code: if 1, Schwarz preconditioning is used, else diagonal preconditioning is used in the CG for the elevation.
<code>tolan</code>	maximum tolerance to recover the pathline in the lagrangian step (in percentage with respect to the average area of the triangles)
<code>teta</code>	degree of implicitness of the scheme; it must have a value between 0.5 and 1 (usually equal to 1)
<code>outbc</code>	type of boundary conditions to be imposed at the outflow
<code>lump1</code>	if 1, stiffness matrix is lumped at Step 2, else consistent matrix is used. This flag is automatically set to 0, whenever <code>turbo=1</code>
<code>lump2</code>	if 1, stiffness matrix is lumped at Step 3, else consistent matrix is used
<code>slip</code>	if 1, free-slip boundary conditions are applied on the wall, else, no-slip conditions are used.
<code>warn</code>	four verbosity levels for the output. Values range from 0 to 3.
<code>video</code>	frequency of output on the standard output
<code>rewrite</code>	frequency of the restart file. A restart file is always written at the end of the calculation.



**iref** time interval (in time steps) between two calls to the  
 adaption procedure; if 0, the adaption is skipped  
**adtype** adaption type; if -1, uniform refine; if 0, refine;  
 if 1, derefine; if 2, adaption;  
**eetype** error estimator; if 1, second derivative of  $\xi$   
 if 2, second derivative of  $v$ ; if 3, mass defect;  
 (see sect. 10.1)  
**reftol** error tolerance fraction respect to the maximum error  
 permitted during the adaption procedure ( $0 < reftol < 1$ )  
**refmax** maximum number of elements permitted during the adaption  
 procedure as a multiple of the elements of the  
 background mesh ( $1 < refmax$ )  
**procs** ignored by the sequential code. Number of processors for the parallel run.  
**subd** ignored by the sequential code. Number of subdomains for the Schwarz  
 preconditioner (if **precond**=1)  
**coarse** ignored by the sequential code. If 1, coarse correction for the Schwarz  
 preconditioner (if **precond**=1)  
**ilut** ignored by the sequential code. If 1, ILUT acceleration for the Schwarz  
 preconditioner (if **precond**=1)

**mesh** It is an ASCII file, where the informations about the mesh are contained. The  
 data structure is the standard one: position of the nodes and list of the connections  
 among the nodes. The informations contained in the **mesh** file are

**ne** number of elements  
**nv2** total number of nodes  
**nv1** number of P1 nodes  
**x(k,j)** k-th coordinate of the node j  
**inod(j)** type of the node  
**lel(k,i)** list of the nodes belonging to element i

These informations are given in the **mesh** file in the following order:

**ne,nv2,nv1**  
**x(1,1),x(2,1),inod(1)**  
**x(1,2),x(2,2),inod(2)**  
 $\vdots$   
**x(1,nv2),x(2,nv2),inod(nv2)**  
**lel(1,1),lel(2,1),...,lel(6,1)**  
**lel(1,2),lel(2,2),...,lel(6,2)**



```

..
lel(1,ne),lel(2,ne),...,lel(6,ne)

```

In the list of the nodes, the P1 are grouped in the upper part of the list; in the connection list, the first three nodes are the P1 nodes listed in counterclockwise sense.

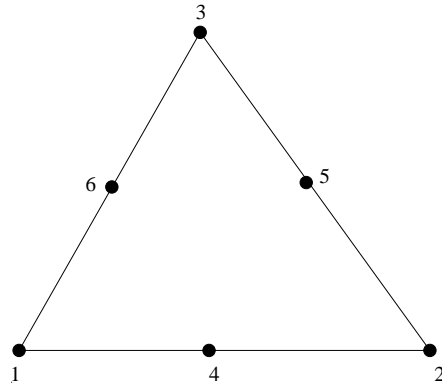


Figure 33: Order of the numbering of the nodes in a triangle.

**bati** This file is read only if **bati=1** in the **datin** file. It contains the bathymetry of each node, when the bottom is not flat. The file is composed by a number of rows equal to the number of nodes, and in each row it is written the water depth of the respective node. In case of constant bathymetry, the depth value is specified in the **datin** file, with the variable **h0**.

**elev.time** This file is read only if **steady=0** in the **datin** file. It contains the Fourier components of the elevation value to be imposed on the boundary.

**disch.time** This file is read only if **steady=0** in the **datin** file. It contains the Fourier components of the discharge value to be imposed on the boundary.

**spy.nodes** This file is read only if **steady=0** in the **datin** file. It contains the list of the spy nodes, that is the nodes for which the value of the transient solution is printed.

**tracer.data** This file is read only if **tracer=1** in the **datin** file. It contains the list of nodes in which the scalar is not zero, together with the corresponding value, and the list of nodes in which the sources are located, together with the value of the sources.



## 15.2 Output

### Output on Video

The output on the standard output of SWEET is printed every `video` iterations. The value of `video` is set in the `datin` file. The standard output of SWEET is the screen, for the sequential code, and the file `proc0.output` for the parallel code. A typical output can be as the following:

```
TIME 20.  sec.; STEP NUMBER = 1
Step 2:  residual= .478D-06 iterations= 62
Step 3:  residual= .958D-06 iterations= 138
residual= .760D-06 iterations= 103
Error Max 0.543D-03 Min 0.271D-03 Average 0.520D-03
xires=.7783D-02 qxres=.8256D-01 qyres=.5788D-01
vxmax=.2823D-01 vymax=.2107D-01 qxmax=.2264D+00 qymax=.1689D+00
cflmax=.6588D-01 frmax=.3184D-02
-18.787 -.154 0.000 0.000 0.000 0.000
0.000 0.000 0.000 0.000 0.000 0.000
-18.9417
```

The meaning of the displayed control parameters is as follows:

<b>residual</b>	is the maximum of the absolute values of the residual; it is always lower than the desired <code>tol</code> value
<b>iterations</b>	is the number of iterations of the linear solver which have been necessary to reach the desired residual
<b>Error</b>	Max, Min, Average are the maximum the minimum and the mean value obtained from the chosen error estimator
<b>xires</b>	maximum value of the magnitude of the difference between the new elevation and the one computed at the previous time step
<b>qxres</b>	maximum value of the magnitude of the difference between the new x-component of the unit-width discharge and the one computed at the previous time step
<b>qyres</b>	maximum value of the magnitude of the difference between the new y-component of the unit-width discharge and the one computed at the previous time step



**vxmax**    maximum value of the magnitude of x-component of the velocity  
**vymax**    maximum value of the magnitude of y-component of the velocity  
**qxmax**    maximum value of the magnitude of x-component of the  
                  unit-width discharge  
**qymax**    maximum value of the magnitude of y-component of the  
                  unit-width discharge  
**cflmax**    maximum value of the velocity CFL number  
**frmax**    maximum value of the Froude number

In the last row of the text displayed on the video, the discharges referring to the open boundaries of the domain are listed. Namely, they are ordered in such a way that the discharges relevant to the 20003, 20004, 20005, 20006, 20007, 20008 type boundaries are listed in the first row, the discharges relevant to the 10003, 10004, 10005, 10006, 10007, 10008 type boundaries are listed in the second row. The value on the last row refers to the sum of the all discharges. Negative values indicates flow entering the computational domain.

It is possible to have additional informations on some numerical and computational features of the code: this is done by setting the **warn** flag value in the **datin** file, according to the following table :

WARN	OUTPUT
0	All the indication written above, plus averaged execution times Parallel run will give also confirmation of the correct starting of all the processors (on standard error unit)
1	As with <b>warn=0</b> plus an indication at the end of every temporal iteration (on standard error unit)
2	As with <b>warn=1</b> plus execution times for every temporal iteration. Warning on any <b>pathline out of boundary</b> are also given on standard error In a parallel run, every processor will produce an output file
3	As with <b>warn=2</b> for a sequential run. Convergence indication for the Schwarz Additive preconditioner are added in every proc.output file
4	As with <b>warn=2</b> for a sequential run. Detailed (and heavy) indications for the Schwarz Additive preconditioner are added in every proc.output file

## Output on File

The output of SWEET is condensed in a unique unformatted file. This file will be written every **rewrite** iterations, with the name **restart.tem.<iteration\_number>**. This file contains :



the physical time at which the values refer to  
 nv2 values of the x-component of the discharge (qx)  
 nv2 values of the y-component of the discharge (qy)  
 nv1 values of the elevation (xi)  
 If **tracer=1**, nv1 values of the passive tracer concentration  
 If **turbo=1**, nv1 values of the k quantity  
 If **turbo=1**, nv1 values of the  $\varepsilon$  quantity

In order to visualize all these quantities, and other of interest, an interactive interface program has been written, named **sweetmtv**. As its name suggests, this program writes the data of the **restart.tem** file in the MTV format, and it visualizes them through the PlotMTV [20] program.

In the case of unsteady computations, SWEET also produces some output relative to the values of the solution as computed in some reference nodes, that have been listed in the **spy.nodes** file. This output is contained in files that are numerated progressively starting from 1001 and on: 1002, 1003, ....

When the adaption is used ( $iref > 0$ ), every time the mesh is changed, a file containing the new mesh, one containing the new bathymetry and a restart file are created. The names of this files are: **mesh.iter**, **bati.iter** and **restart.tem.iter**; where iter is the time step index. The content of the last two files has already been described. In the first file are contained all the informations of a usual mesh file, and in addition informations about how to rebuild the final mesh starting from the background mesh.

The additional informations in the **mesh.iter** file, are given in brackets, as follows:

```

ne,nv2,nv1
x(1,1),x(2,1),inod(1)
x(1,2),x(2,2),inod(2)
...
x(1,nv2),x(2,nv2),inod(nv2)
lel(1,1),lel(2,1),...,lel(6,1) [ETYPE(1),E_ID(1)]
lel(1,2),lel(2,2),...,lel(6,2) [ETYPE(2),E_ID(2)]
...
lel(1,ne),lel(2,ne),...,lel(6,ne) [ETYPE(ne),E_ID(ne)]
[*****]
[** END OF STANDARD MESH FILE; WHAT FOLLOWS IS THE HISTORY FILE **]
[*****]
[NELI,NVI,NELF,NVF,LAST_LEVEL,PHISTORY]
[0 0 0 THIS IS THE 1 .TH LEVEL OF REFINEMENT]
[phistory,e1,e2,e3,e4,e1_id,e2_id,e3_id,e4_id]
[0 0 phistory THIS IS THE 2 .TH LEVEL OF REFINEMENT]
[phistory,e1,e2,e3,e4,e1_id,e2_id,e3_id,e4_id]
...

```



where the `ETYPE(i)` is the type of the  $i$ .th element and `E_ID(i)` its identifier; `NELI` and `NVI` are number of elements and of P1 nodes in the background mesh; `NELF` and `NVF` are number of elements and of P1 nodes in the new mesh; `PHISTORY` is the pointer to the last element contained in the history tree; `phistory` is the pointer to the current element in the history tree; `e1,e2,e3,e4` are indices of the four elements obtained from a standard sub-division of an element and `e1_id,e2_id,e3_id,e4_id` are the corresponding identifiers. For a more detailed description of these variables see sect. 14.

## 16 The Parallel Setup

In this Section we illustrate how to setup the input for a parallel run, starting from the input for the sequential version of SWEET. The parallel code needs much more informations than the sequential code, so the input system is more elaborated. However, it has been followed the strategy to maintain some crucial input and output files, like the `restart.tem` restart files, so to have the maximum compatibility with the sequential input.

### 16.1 Partitioning the Mesh

In order to partition the mesh, we make use of a public domain software call Chaco [9]. Other packages are available, for example Metis [11] and TopDomDec [10]; the user can freely chose the software he prefers. It must be noted that Metis uses the same input and output format used by Chaco and so the two programs are freely interchangeable, while TopDomDec adopts a different data format. We will refer, in the following, solely to the Chaco package. Any partitioning algorithm contained in Chaco can be used. It is particularly hard to say if an algorithm works better than the others, the behaviour depending much on the shape of the original integration domain. As a tendency, we have noted that good partitions are created by the Spectral Bisection and by the Kernighan-Lin algorithms. The Chaco program works using informations on the graph of the mesh. To build the input file for Chaco, we must first run a program called `before`, which creates a file called `graph` in the Chaco input format. The program `before` reads as input the `datin` and the `mesh` input files of the scalar code. The Chaco package creates a file whose name must be `partition`. The same file is read by the program `after`, which creates the input file for the parallel SWEET code analogous to the `mesh` file for the sequential version of the code. The file is thus called `pa_mesh`, with clear significance.

The `pa_mesh` file contains indication only on the first level of subdomains (the one on which act all the explicit steps). To create the second level of partition and the relative informations, we must use different preprocessing codes. First of all, we must use the code `matrix`, which creates the files to be used by the subsequent program `setup`. The program `setup` reads the number of subdomains for the second level-partition in the file `datin`.



The program **setup** creates a series of input files for the different processors involved in the calculations. The total number of these files depends on the number of processors, and their size depends on the total number of sub-domains. When a large number of sub-domains is requested, the time needed by the **setup** code can be quite long, up to several minutes. This time depends also on the total number of nodes of the global mesh.

Now we have all the input files for a run of our code: let's briefly summarize what the program needs:

- **datin** file
- **bati** file, if needed (**bati**=1 in **datin**)
- **pa\_mesh** file, created by **after**
- **dat\*.tmp** files, created by **setup**
- **elev.time**, **disch.time** and **spy.nodes** if needed (**steady**=0 in **datin**)
- **restart.tem** if requested (**rest**=1 in **datin**); this file can be created both by the sequential and the parallel version of SWEET

Every time that one wants to change the initial conditions of the problem, or the output level of the code, or the choice of the preconditioning, then the file **datin** must be modified, by hand.

Every time that one wants to change the number of the subdomains for the second-level partition, he must modify the **rc.run\_vars** file and rerun the **setup** code.

Every time that one wants to change the number of the subdomains for the first-level partition, he must rerun the **chaco** code, and then the **after** and the **setup** codes.

Every time that one wants to change the mesh, then he must recreate the whole input system, starting from the **matrix** code.

A sketch of the dependency relations of the input files is given in Figure 34.

To deal with the managing of the input files, the Unix **make** command is of great help; with a simple **makefile** file like the one shown in the following, it will be necessary only to launch **make** and the entire cascade of programs will produce in few seconds all the input files needed by the program, without any other external intervention.

```
all :  rhs.dat graph partition dat_mtrx_m01_p001.tmp pa_mesh
rhs.dat :  mesh
          matrix
graph :  mesh
        before
partition :  graph
```



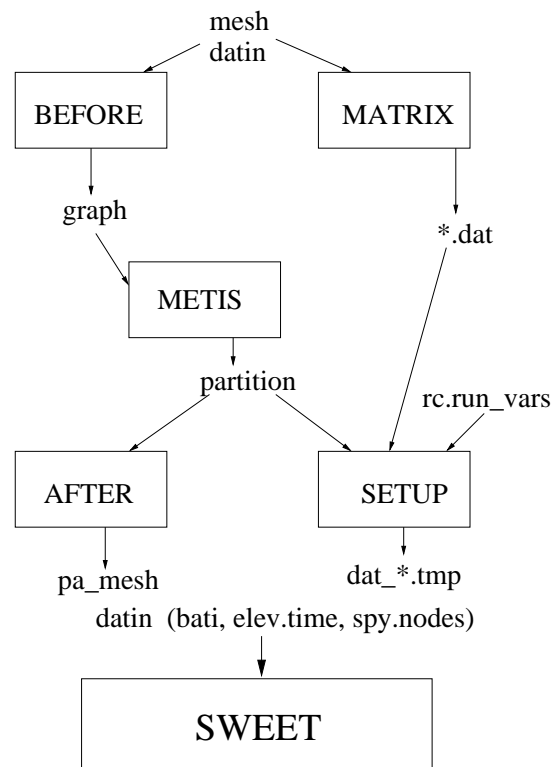


Figure 34: Relations between the input files and the pre-processing programs for the SWEET code. Programs are represented in boxes, plain names refers to input/output files.



```

chaco
dat_mtrx_m01_p001.tmp : partition rc.run_vars
                        setup
pa_mesh : partition
        after

```

## 17 The Parallel Run

The SWEET code use the PVM message passing library, so the PVM procedure for running a PVM code must be followed. See Appendix A for a PVM resume.

It is not possible to run the parallel code on a single processor. The minimum partition is composed by 2 *first-level* subdomains and 2 *second-level* subdomains, running on two processors. It must be kept in mind that the number of *first-level* subdomains must be equal to the number of processors and that the number of *second-level* subdomains must be equal or greater than the number of processors.

Before running a long simulation, the behaviour of the selected combination of parameters, both physical as well numerical, must be checked. The speed of the code can be strongly influenced by the number of subdomains used in the Schwarz preconditioning and by the quality of the partition. Sometimes, a bad partition of the original mesh can lead even to non-convergence of the global CG, in dependence of the chosen preconditioner.

If a problem is too big to fit on the selected pool of processors, other processors must be added to the pool, when possible. The code is capable to run about 25000 nodes per processor, in double-precision, considering 128 MB of RAM per node (i.e. the standard IBM/SP2 configuration).

Some error messages are redirected to the standard error, some other are signaled in the output files: check both the devices to monitor the run.

When the run is completed, always wait for the

PVMe: new epoch

signal to access the output files.

### 17.1 The Parallel Output

**Warning:** this section only contains the differences between the sequential and parallel output. Please read first the Section 15.2, to understand the output informations of the SWEET code.

There are some differences between the output files produced by the sequential and the parallel version of SWEET. This is primarily due to the fact that every processor produces distinct output files. However, when some global informations have to be collected into a



file, like the `restart.tem.*` files, the parallel program will produce unique files, just like the sequential program.

All the output files are written in the working directory.

The `restart.tem.*` restart files are fully compatible with the ones produced by the scalar one.

The files to monitor the spy nodes have the same format than the sequential ones, but with different names: while the name in the sequential code are `2001, . . . 2020`, after a parallel run the files will have names like `XXYY` where `XX` indicates which processor has written the file (from 1 to 99), and `YY` is the number of the spy node (from 1 to 20). When a spy node is shared between two processors, then two identical files are produced (with different names).

The standard output of the sequential run is now directed to a file called `proc0.output`. This file is always written, even when the output level (`iwarn` flag in `datin` file) is set to zero. When `iwarn` is greater than one, each processor writes an output file, named `procX.output`, where `X` is the processor number.

## 18 Practical Remarks

We add here some practical remarks about the questions that can arise when using SWEET to simulate real-life flows.

### 18.1 Hints

Which **time step** should I choose?

From strictly physical arguments we can say that the time step `dt` should not necessarily be larger than  $10^{-1} - 10^{-2}$  times the characteristic time of the phenomena we are interested in. From a numerical point of view, an upper bound can be imposed because of stability reasons. In particular, if mass matrix lumping is adopted at Step 2, it must be verified that  $\frac{2\Delta t \nu}{\Delta x^2} < 1$ . Moreover, for the lagrangian integration of the convective terms, it must be ensured that `cflmax` < `rk`, that is the pathline must not require more than `rk` steps to be reconstructed. For steady state computations the time step should be chosen only according to stability reasons.

**Pathline out of boundary:** what does it mean?

This message (given on the standard error only if `warn` is greater than one), indicates that the lagrangian integration is failed on a given node. Thus, it can be considered as an inaccuracy indicator. The tolerance for this kind of inaccuracy is left to the user, in the sense that it is the user himself that has to judge on how many nodes it is possible to ignore the advection contribution.

It is possible to augment the accuracy by increasing the `rk` value, that is the number of steps in which the lagrangian integration is performed, and/or by decreasing the `dt`



value.

Which **eddy viscosity** and **Strickler coefficient** should I choose?

In a 2D approach, the stress on the bottom can be only modeled and not actually simulated. The Strickler coefficient depends on the nature of the bottom, and standard tables yield values experimentally deduced, typically ranging between 30 and 100. Usually the eddy viscosity coefficient has a secondary importance in the equations, not being necessary to use its stabilizing numerical effect in the SWEET approach; typical values for it are 0.1-2 for simulations in river, few hundreds for simulations in large areas (coastal regions). The eddy viscosity is usually tuned by comparison of the numerical results with experimental measures. For numerical reasons, it is necessary that the eddy viscosity is not zero when mass matrix lumping is adopted.

Remember that if the  $k - \varepsilon$  model is used (**turbo=1**), then the value for the eddy viscosity is changed through the calculation, according to the model.

How do the results of the simulation depend on **initial conditions**?

The initial conditions are often unknown in real life simulations. When one is interested in the steady state behavior, any initial condition can be used, unless it is not so extreme to yield to instabilities in the computation. When considering unsteady flow, for instance because the boundary conditions change in time, usually the only reasonably initial condition is to start from the steady state solution related to the boundary conditions at time zero.

Which is the minimum **tolerance** of the residual to get acceptable results?

The residual compared with **tol** is the maximum value of the absolute value of the residual. As an error of 1% can be usually accepted in this kind of simulations, that involve uncertainty for a lot of physical parameters and assumptions in the chosen model, it is suggested to imposed a value of **tol** which is one thousandth of the typical value of the unknown. For instance, if the elevation of the water is expected to change in the computational domain for few centimeters, a tolerance of  $10^{-4}$  can be confidently used.

What difference in the results is expected to be found when using mass matrix **lumping**?

The numerical results computed using mass matrix lumping are less accurate than when using consistent mass matrix. This is because mass matrix lumping corresponds to using a lower order quadrature rule in evaluating integrals. Moreover, mass lumping involves explicit discretization of the diffusive term, so that the limitations  $\frac{2\Delta t\nu}{\Delta x^2} < 1$  must be observed. It is suggested to perform preliminary calculations by lumped approach, in such a way to tune appropriately the parameters, and then to use the consistent mass matrix for final computations.

Which kind of **parallel preconditioner** should I use for the solution of the linear system?

Since there is not an universal choice, the code asks for specification about the parallel



preconditioner. Two possibilities are implemented in the parallel SWEET code: a diagonal preconditioner and an additive Schwarz preconditioner. The Schwarz preconditioner is always the most effective algorithm in reducing the number of global CG iterations. However, its computational cost is high, and it can be slower than the diagonal preconditioner. This latter situation occurs when the matrix of the linear system is not enough ill-conditioned to represent a difficult task for the global CG. Low number of unknowns, smooth bathymetry, small time steps, are all indices of relatively “easy” problems; nevertheless, the only mean to determine the best choice is always to test both the preconditioners on the given problem. The choice of the preconditioner can be influenced also by the particular parallel hardware on which the code runs. In a very schematic way, we can say that the Schwarz preconditioner is particularly suitable when the parallel system has poor communication performances relatively to its computational speed, since the Schwarz algorithm greatly reduces the amount of communication requested by the CG algorithm. The diagonal preconditioning is in principle a better choice when the processors are connected through a very efficient network, so that communication overhead is small.

## 18.2 When Everything Else Fails...

...please contact:

Luca Paglieri  
e-mail : [luca@crs4.it](mailto:luca@crs4.it)  
Phone : 39 - 70 - 2796316  
Fax : 39 - 70 - 2796302

CRS4 : Centre for Research, Development and Advanced Studies in Sardinia  
via N. Sauro, 10  
09123 Cagliari  
Italy



## A PVM Quick Guide

This is a quick guide to PVM [17]: it deals only with the case of PVMe 2.1 on a IBM/SP2 system, with 4.1 Operative System Level.

PVM is a system composed by a message-passing library and an underlying software running on every machine of the parallel system. In order to be able to use PVM, the software must be started on the chosen set of processors, and the library must be linked to the other object files to form the executable.

PVM is a public software. PVMe is a proprietary version of PVM, made by IBM for its hardware systems. It is nearly fully compatible with PVM, and, on the parallel systems SPx, it has been designed so to use the High Performance Switch, to enhance its performance. Differently from PVM (which runs on the IBM systems as well), PVMe runs on the SPx nodes in an exclusive way: only a single PVMe daemon can run on a node. Thus, only a user at a time can access the specified node(s). For this reason, the PVMe daemon must be stopped when one is not going to use it for some time, since otherwise the nodes on which the daemon runs will remain inaccessible to the other users.

### A.1 Starting PVMe

The first thing to do is to select a pool of nodes and create a file named, as example, **hostfile**, containing the names of the chosen nodes, one per row, **without** any blank row.

Example:

```
isp1n1.sp2.cris.enel.it
isp1n4.sp2.cris.enel.it
isp1n5.sp2.cris.enel.it
```

At this point, run

```
pvme hostfile
```

You should have an output like the following:

```
PVMD:
```

```
Assuming default as control workstation.
```

```
PVMD:
```

```
Trying to get 3 nodes.
```

```
PVMD: Using isp1n1 with dx=/usr/lpp/pvme/bin/pvmd3e, ep=/u/sweet/pvm3/bin/RS6K.
```

```
PVMD: Using isp1n4 with dx=/usr/lpp/pvme/bin/pvmd3e, ep=/u/sweet/pvm3/bin/RS6K.
```

```
PVMD: Using isp1n5 with dx=/usr/lpp/pvme/bin/pvmd3e, ep=/u/sweet/pvm3/bin/RS6K.
```

```
PVMD:
```

```
Ready for <3> hosts.
```



The name  
`/usr/lpp/pvme/bin/pvmd3e`  
indicates the full path of the PVMe daemon, while  
`/u/sweet/pvm3/bin/RS6K`  
indicates the directory containing the PVM executables.

Now the pvme console is started, and you should have the prompt

`pvme>`

this is the PVMe-console prompt, it is **not** a shell prompt, and only PVM special commands can be executed from this prompt. If, in the starting operation, any error message appears, type immediately from the PVMe prompt the command

`halt`

and restart the PVMe. If the message persists, then consult your system administrator.

Let's suppose that you have successfully started the PVMe console and that now you have the PVMe prompt. Try to type

`help`

this will show you all the PVMe special commands, together with a brief explanation. The main commands that you will probably encounter are:

- **quit** : exits the PVMe console, returning to the unix prompt. This operation leaves the PVMe daemon (pvmd3e) running in batch mode on all the nodes contained in the `hostfile` file. You will have the message  
`pvmd still running`  
indicating that everything is ok. PVMe is a software which normally runs in batch mode, so this is the standard operational mode. From ANY unix prompt on ANY node of the partition you can reactivate the PVMe console (and thus the PVMe prompt) by simply typing  
`pvme`  
After this, you must have the message  
`pvmd already running`  
indicating that the PVMe daemon is already alive. If you do not receive this message, then, for some reasons, the daemon has been killed. If this is the case, type, from the PVMe prompt, the command  
`halt`  
and re-run the command  
`pvme hostfile`  
to start again the daemon on every node of the partition.
- **halt** : stops the PVMe daemon on all the nodes of the partition, and then stops the PVMe console. It stops also every PVM process running on the nodes. After this, you must rerun the PVMe daemon from the start.
- **reset** : kills all the PVMe jobs running on all the nodes of the partition, leaving untouched the PVMe daemon. Use this command **every time** that your PVM job



aborts for any reason. You should have the signal

**New epoch <number>**

indicating that everything is ready for a new PVM job.

When the PVMe daemon is properly running on the partition, it is possible to run the application. Consider that if you don't give an absolute path for the executable, then PVM assumes that the executable is in the

`$HOME/pvm3/bin/RS6K/`

directory.

## A.2 PVM Messages

Both PVM and the specific program that use PVM can give some messages during the execution of the run. A PVM job will run on every node of the partition: we thus have to think to have several programs running together, but completely independent one from the another (except that for communications). When one runs the application, a single program on a given node is started. This program then “spawn” the other programs, one for each of the remaining nodes of the partition. The standard output and the standard error for the “father” program are the shell from which it has been executed. For the other programs, the output and error go to the shell from which the PVMe console has been started. Note that the two shell can be the actually the same (this is the normal situation), so all the output will be mixed together. Usually, PVMe puts an indication of the node that gives a particular output, by writing the name of the node before the message.



## References

- [1] Agoshkov, V.I., Ambrosi, D., Pennati, V., Quarteroni, A., and Saleri, F.; *Mathematical and Numerical Modelling of Shallow Water Flow*, Computational Mechanics, **11**, 1993.
- [2] Ambrosi, D., Corti, S., Pennati, V., and Saleri, F.; *Numerical simulation of the unsteady flow at the Po river delta*, J. of Hydraulic Engineering, ASCE, to appear.
- [3] Quarteroni, A., and Valli, A.; “Numerical approximation of partial differential equations”, Springer Verlag, 1994.
- [4] Walters, A.; *Numerically induced oscillations in the finite element approximations to the shallow water equations*, Int. J. Numer. Meth. Fluids, **3** 1993.
- [5] Zienkiewicz, O.C., and Taylor, R.L.; “The finite element method”, Mc Graw-Hill 1989.
- [6] Benqu , J.P., Cunge, J.A., Feuillet, J., Hauguel, A., and Holly, F.M.; *New method for tidal current computation*, J. of Waterway, Port, Coastal and Ocean Engineering, **108**, 1982.
- [7] Pironneau, O.; *On the Transport-Diffusion Algorithm and its Application to the Navier-Stokes Equations*, Numerische Mathematik, **38**, 1982.
- [8] Cai, X.C.; *A family of overlapping Schwarz algorithms for non-symmetric and indefinite elliptic problems*, in “Domain-based parallelism and problem decomposition methods in computational science and engineering”, SIAM, 1994.
- [9] Hendrickson, B., and Leland, R.; *The Chaco user’s guide, Version 1.0*, Sandia Technical Report, **SAND93-2339** 1993.
- [10] Sharp, M., and Farhat, C.; “TOP/DOMDEC User’s Manual”, PGSoft and The Regents of the University of Colorado, 1995.
- [11] Karypis, G., and Kumar, V.; *Metis: Unstructured graph partitioning and sparse matrix ordering system*, University of Minnesota Technical Report, 1995.
- [12] Chan, T.F., and Mathew, T.P.; *Domain decomposition algorithms*, Acta Numerica, 1994, pag. 61-143.
- [13] Koobus, B., Lallemand, M.H., and Dervieux, A.; *Unstructured Volume agglomeration MG; solution of the Poisson equation*, Rapport de recherche RR-1496, INRIA (FR), (1993).



- [14] Lallemand, M.H, Steve, H., and Dervieux, A.; *Unstructured multigriding by volume agglomeration: current status*, Computer and Fluids, **21** (3), 397-433 (1992).
- [15] Saad, Y.; "Iterative Methods for Sparse Linear Systems", PWS Publishing Company, (1996).
- [16] Hinkelmann, R., and Zielke, W.; *A parallel three-dimensional Lagrangian-Eulerian model for the shallow water and transport equations*, "Computational methods in water resources XI", A.A. Aldama et al. eds., Computational Mechanics Publications (1996).
- [17] Beguelin, A., Dongarra, J., Geist, G.A., Manchek, R., and Sunderam, V.; *A user's guide to PVM: Parallel virtual machine*, Technical report TM-11826, Oak Ridge National Laboratories (1991).
- [18] Ambrosi, D., Corti, S., Pennati, V., and Saleri, F.; *A 2D numerical simulation of the Po river delta flow*, in "Modelling of Flood Propagation Over Initially Dry Areas", Molinaro P. and Natale L. eds. (1994)
- [19] Falconer, R.A.; *Numerical modeling of tidal circulation in harbors*, Journal of Waterway, Port, Coastal and Ocean Division ASCE, **106**, n.WW1, pp.31-48 (1980)
- [20] Toh, K.K.H.; *The MTV plot data format*, Visualization Working Group, Intel Corporation (1993)
- [21] Rodi, W.; *Turbulence models and their application in hydraulics: a state of art review*, IAHR Monography Series (1993)
- [22] W.G. Habashi, M. Fortin, J. Dompierre, M-G. Vallet, and Y. Bourgault. Certifiable CFD through mesh optimization. *submitted to AIAA Journal*, pages 1-22, 1996.
- [23] R.A. Walters and E.J. Barragy. Comparison of  $H$  and  $P$  finite element approximations of the shallow water model. *Int. J. Numer. Meth. Fluids*, 24:61-79, 1997.
- [24] R.E. Bank and A. Weiser. Some a posteriori error estimators for elliptic partial differential equations. *Mathematics of Computation*, 44(170):283-301, April 1985.
- [25] R.E. Bank. *PLTMG: A software package for solving elliptic partial differential equations. Users' guide 7.0*. SIAM, 1994.
- [26] R. Lohner. Finite element methods in CFD: grid generation, adaptivity and parallelization. In *Unstructured grids methods for advection dominated flows*. AGARD-R-787, 1992.
- [27] C. Johnson. *Numerical solution of partial differential equations by the finite element method*. Cambridge University Press, 1987.



- [28] R. Sacco and F. Saleri. Mixed Finite Volume Methods for Semiconductor Device Simulation. *Numerical Methods for Partial Differential Equations*, 3(13):215–236, 1997.
- [29] T. Utnes. Finite element modelling of quasi-three-dimensional nearly horizontal flow. *Int. J. Numer. Meth. Fluids*, 12:559–576, 1991.
- [30] V. Casulli and Cheng R.T. Semi-implicit finite difference methods for Three dimensional shallow water flow. *Int. J. Numer. Meth. Fluids*, 15:629–648, 1992.
- [31] V. Rudiger. *A Review of A Posteriori Error Estimation and Adaptive Mesh Refinement Techniques*. Wiley Teubner, 1996.
- [32] L. Formaggia and F. Rapetti. *MeSh2D, Unstructured Mesh Generator in 2D, version 1.0. Algorithm overview and description*. CRS4 Cagliari, February 1996.
- [33] A. Balzano, R. Pastres, and C. Rossi. In *Coupling hydrodynamic and biochemical mathematical models for lagoon ecosystem*. XI Int. Conf. on Comp. Meth. in Water Resources, Cancun, Mexico, 1996.
- [34] Various. *Handbook of Grid Generation*. CRC Press, 1997.
- [35] R.S. Chapman and C.Y. Kuo, *Application of the two dimensional  $k - \varepsilon$  turbulence model to a two dimensional steady free surface flow problem with separation*, *Int. J. Numer. Meth. Fluids*, **5**, pp.257-268, 1985
- [36] D.E. Abbott and S.J. Kline, *Experimental investigation of subsonic turbulent flow over single and double backward facing step*, *Journal of Basic Engineering, Transactions ASME*, **84** (1962)